The Influence of Soluble Fragments of Extracellular Matrix (ECM) on Tumor Growth and Morphology

Nurun N Nargis*, Ralph C Aldredge*, Robert D Guy**
*Department of Mechanical and Aerospace Engineering
**Department of Mathematics
University of California, Davis, CA 95616, USA

Abstract

A major challenge in matrix-metalloproteinase (MMP) target validation and MMP-inhibitor-drug development for anti-cancer clinical trials is to better understand their complex roles (often competing with each other) in tumor progression. While there is extensive research on the growth-promoting effects of MMPs, the growth-inhibiting effects of MMPs has not been investigated thoroughly. So we develop a continuum model of tumor growth and invasion including chemotaxis and haptotaxis in order to examine the complex interaction between the tumor and its host microenvironment and to explore the inhibiting influence of the gradients of soluble fragments of extracellular matrix (ECM) density on tumor growth and morphology. Previously, it was shown both computationally (in one spatial dimension) and experimentally that the chemotactic pull due to soluble ECM gradients is anti-invasive, contrary to the traditional view of the role of chemotaxis in malignant invasion [1]. With two-dimensional numerical simulation and using a level set based tumor-host interface capturing method, we examine the effects of chemotaxis on the progression and morphology of a tumor growing in nutrient-rich and nutrient-poor microenvironments which was not investigated before. In particular we examine how the geometry of the growing tumor is affected when placed in different environments. We also investigate the effects of varying ECM degradation rate, the production rate of matrix degrading enzymes (MDE), and the conversion of ECM into soluble ECM. We find that chemotaxis due to ECM-fragment gradients strongly influences tumor growth and morphology, and that the instabilities caused by tumor cell proliferation and haptotactic movements can be prevented if chemotaxis is sufficiently strong. The influence of chemotaxis and the above factors on tumor growth and morphology are found to be more prominent in nutrient-poor environments than in nutrient-rich environments. So we extend our investigations of these antinvasive chemotactic influences by examining the effects of cell-cell and cell-ECM adhesion and low proliferation rate for tumors growing in low-nutrient environments. We find that as the extent of chemotaxis increases, the effects of adhesion on tumor growth and shape become negligible. Under conditions of low cell mitosis, chemotaxis may cause the tumor to shrink, as the extent of chemotaxis increases. Both stable and unstable tumor shrinkage are predicted by our model. Unexpectedly, in some cases chemotaxis may contribute toward developing instability where haptotaxis alone induces stable growth.

1. Introduction

Cell motility, coupled with cell proliferation and regulated adhesion to the extracellular matrix (ECM), and degradation of ECM molecules, allows an invading tumor cell to move through the surrounding tissue [2, 3]. The ECM, a substantial component of tissue, consists of an interlocking mesh of fibrous proteins and polysaccharide including collagen, elastin, laminin, fibronectin and hyaluronan. ECM acts as a supporting structure to which cells can anchor and generate force. The state of macromolecules within the ECM is of critical importance and proteolysis is a major factor leading to changes in the ECM [4]. Cancer invasion involves the over-expression of proteolytic matrix degrading enzymes (MDEs), such as the urokinase-type plasminogen activator (uPA) and matrix metalloproteinases (MMPs). Although overexpression of MMPs correlate with poor prognosis in cancer patients, pharmaceutical inhibitors of MMP have failed clinically [5-9]. The reasons for failure can be the broad-spectrum activity of the inhibitors used, using inhibitors

during the latter stage of cancer, the opposite effects (pro-invasive and anti- invasive) exerted by MMPs on cancer progression [10] and altered signaling activities exhibited by MMPs during tumorigenesis [7]. The failure from the clinical trials has shed light on the diverse proteolytic activities involved during different steps of tumor progression and paved the way to explore underappreciated functions of proteases. The major challenge is to differentiate the action of MMPs that promote tumor growth and invasion from those that are crucial for host defense, as blocking the latter will worsen the clinical outcome [7].

A variety of soluble and substratum-bound factors influence directed cell migration at different stages during tumor invasion and metastasis. Haptotaxis is the directional motility of cells, usually up gradients of cellular adhesion sites in the ECM created through the degradation of the ECM by MDEs secreted by tumor cells. Chemotaxis is defined as cellular locomotion directed in response to a gradient of a soluble chemical factor. During the process of tumor invasion, proteolytic degradation also results in solubilisation of ECM components [11, 12] which induce chemotactic movement due to the gradients of soluble ECM fragments. Perumpanani et al. [1] showed that in the human fibrosarcoma cell line HT1080, MMP-2-digested fragments of fibronectin exert a chemotactic pull stronger than that of intact fibronectin. As the gradient in degraded fragments is opposite to that of the direction of invasion, the chemotaxis due to these soluble fragments actually inhibits invasion. Thus, an optimally invasive phenotype corresponds to a balance between MMP production and inhibition, and the relative proportions of digested and intact ECM components. Therefore the therapeutic use of MMP inhibitors (MMPIs) against tumors expressing high levels of MMP could produce an augmentation of invasion. Klominek et al. [13] reported that ECM proteins with molecular weight greater than 220,000 has both chemotactic and haptotactic properties, while the proteins with molecular weights of approximately 67,000 have chemotactic and chemokinetic (random motility) but not haptotactic properties. The importance of both pro- and anti-invasive properties of various proteases in cancer, which, depending on the circumstances, may either suppress or promote tumor growth are discussed in [8, 10, 14-16]. Nonetheless, the mechanisms by which these proteases exert their pro- or anti-invasive properties are largely unknown and represent a challenging issue for the near future [10].

Mathematical modeling has the potential to provide insight into tumor growth and invasion through systematic studies of fundamental constituent processes [17] and thereby reducing the number of costly experiments needed for the development of therapies. The effects of nutrient concentration (in the microenvironment) on shape instabilities of tumor growth has been investigated using level set methods [17-22]. Instability provides a mechanism for tumor invasion that does not require development of a neovasculature to supply essential nutrients. Poplawski et al. [23, 24] demonstrated that the development of instability depends primarily on the diffusional limitation parameter (ratio of tumor growth rate to diffusion rate of nutrients) while the morphological details depend on cell–cell adhesion. The lack of competition for nutrients (high nutrient environment) promotes spherical, noninvasive tumors. Low concentrations of nutrients (which cause tumor-cell competition), or cells with a very high nutrient-consumption rate generate a fingering instability and irregular, invasive tumors. Their results agree with the in vitro and in vivo experiments conducted in [3, 25-27] and with other tumor-models predictions without considering haptotaxis [17, 20, 21, 28-30] and with haptotaxis [31-33]. Simulation results show that increases in both MDE secretion rate and the haptotaxis coefficient promote invasion [34] and inhibiting haptotaxis or the proteolysis result in less disperse invasion fronts [35] which is found in vitro case as well.

Anticancer therapies are divided into two broad classes: antiproliferative (chemotherapy) and anti-invasive therapy. Chemotherapy uses cytotoxic drugs to either slow down or block the cell division cycle causing cell death by attacking rapidly growing cells. Two chemotherapy protocols are used: (i) a series of scheduled doses administered into the blood stream (free drug delivery) or (ii) releasing a drug at a constant rate through nanoparticles [36]. The Mathematical model based on first principles of cell biophysics, drug pharmaco-kinetics and drug pharmaco-dynamics developed by Pascal et al. [37] suggests that a continuous infusion of nanocarrier-mediated drug is more effective than scheduled doses because of the higher uptake

rate and hence lower amounts of drug are required to kill the same amount of cells due to improved cellular uptake rates. The time-dependent model [37] is extended in [38] by accounting for spatial dependence in order to predict tumor response to different kinds of drug delivery methods (nano-vectored drug and free drug delivery). Model predictions are also validated using experiments on an in vivo breast cancer mouse model with different drug delivery methods. By combining mathematical modeling with experiments in mice for predicting chemotherapy drug response, Frieboes et al. [39] showed that the drug response in mice (represented by the fraction of dead tumor volume) can be predicted from drug transport characteristics (blood volume fraction, average geometric mean blood vessel radius, drug diffusion penetration distance, and drug response cell culture). Koay et al. [40] developed **a** mass transport model for measuring mass transport properties to describe qualities of the pancreatic tissue and its surrounding vasculature during routine contrast-enhanced CT scans of human pancreatic ductal adenocarcinoma (PDAC). This clinical study based on discrete radiographic features of the PDAC showed that high stromal density inhibits incorporation of drug mediated by hENT1 (human equilibrative nucleoside transporter 1) into the tumor. The mechanistic model based on the physical laws of diffusion in [41] can accurately predict the fraction of tumor cells killed from chemotherapy in patients with glioblastoma and colorectal cancer metastatic to liver based on parameter values that are measurable in clinical test.

Regarding anti-invasive therapies, it was shown in [42] that in the presence of gradients of both soluble and fixed ECM gradients, inhibiting only haptotaxis could be inefficient. Berry et al. [43] presented a kinetic model that describes the interactions between ECM proteins, proteinases, proteolytic fragments, and integrins and focused on the role of the cryptic functions displayed by the proteolytic fragments of ECM in cell invasion. Another molecular-level model developed by this group is based on ECM remodeling using the kinetics of a proteinase/transglutaminase cycle interconverting insoluble ECM and soluble proteolysis fragments [44]. However the chemotaxis due to soluble fragments were not considered in those models [43, 44]. Hacker [45] presented a mathematical model for the interactions of cells with ECM fiber network where metastatic tumor cells move due to anisotropic diffusion, haptotaxis (due to the gradients of undissolved adhesion sites in the ECM network) and chemotaxis (due to the solute network fragments, produced from proteolysis, and the epidermal growth factor which may guide the cells to a blood vessel). Numerical simulations were carried out in two space dimensions for different ratios of diffusive and chemotactic strength with and without haptotaxis. However this study assumed that tumor cells are neither proliferating nor apoptotic, so the effects of nutrient concentration were not included in the model.

To date, no experimental or computational work has elucidated the motility retarding effects of digested fragments of ECM on tumor growth and morphology including cell proliferation and the effects of nutrient concentration in the microenvironment. Because these chemotactic gradients are soluble they would eventually be dissipated, resulting in continued invasion, although at a lower rate [1]. Our hypothesis is that the tumor morphology will change significantly due to the cell migration towards the chemotactic pull associated with the gradients of soluble fibronectin fragments. So we model tumor growth and invasion due to directed cell motion and investigate the role of chemotaxis and related biophysical parameters on tumor growth and morphology with the variations of nutrient availabilities in the microenvironment. In our model, cell motion depends on oncotic pressure from cell proliferation, adhesion forces between cells and between cells and the ECM, the relative strength of chemotaxis and haptotaxis due to the gradients of soluble ECM and insoluble ECM, respectively. Using two-dimensional numerical simulations, we present the results of a parameter study of quantitative aspects of the tumor progression, such as the size and shape of tumors with a range of biophysical and chemotaxis parameters, and investigate the causal link between these parameters on tumor growth and morphology. Our study stands out from previous mathematical investigations in the following ways:

(i) While earlier mathematical models have examined the enhancement effect of MMP (by

haptotaxis) on tumor growth and morphology; our model is the first to investigate the inhibitory effects of MMP (by chemotaxis) with variations of nutrient concentrations in the microenvironment (nutrient-rich and nutrient-poor microenvironments).

(ii) We include tumor-cell motion due to cell-proliferation (primary source of cell movement) and cell-cell and cell-ECM adhesion pressure in our chemotaxis model, not included earlier.

(iii) We investigate the influence of chemotaxis due to soluble-ECM gradients, for tumors growing in hypoxic environments with varying extents of cell adhesion

(iv) The influences of chemotaxis and haptotaxis on tumor growth dynamics and morphology under conditions of low cell proliferation in a low-nutrient environment are investigated here.

The various influences of fragments of ECM through chemotaxis on tumor growth and morphology predicted by our study, might partially explain why the MDE inhibitors have not been successful as therapeutic agents in clinical trials. Especially, we show that the tumor morphology is unstable with increase in ECM degradation rate if the chemotaxis coefficient is not strong enough and chemotaxis may contribute to the initiation of the instability for low proliferation environment. Our model can predict the tumor growth and morphology due to both promoting and inhibitory effects of MMP with variations of tissue environment and will, therefore, be helpful to design combination therapies including selective MMP inhibition.

2. The Mathematical Model

There are two major approaches for tumor growth modeling: the first employs continuum models to describe the evolution of the tumor in terms of systems of partial differential equations; the second approach uses discrete models. A one-millimeter-radius spheroidal tumor contains around one million cells. In large scale systems continuum models are more suitable than discrete-cell models. In a continuum model, the cell velocity is obtained from the inertia-less momentum-conservation equation based on Darcy's law, representing the instantaneous equilibrium among forces associated with pressure, cell adhesion, elastic forces, forces exchanged with the ECM leading to haptotaxis and chemotaxis due to gradients of nutrient/growth factors, and other mechanical effects [46]. The adhesion among cancer-cells is modeled by a surface tension at the tumor surface [17, 20, 21, 28, 46-55]. Our study employs a continuum model based on previous continuum model of solid tumor growth [19] but is extended here to take into account cell motion due to chemotaxis. Following [1], our model assumes that a sharp interface separates the tumor from the host tissue and the total density of tumor cells is constant in the tumor interior and drops sharply to zero in the tumor exterior, We neglect necrosis while accounting for apoptosis (programmed cell death). Although we do not include the tumor blood flow and necrosis, our model can be extended to incorporate these effects.

We model a single vital nutrient (oxygen) which is required for cell survival and mitosis. Let D be a rectangular domain (Figure 1) containing the tumor mass Ω_T and the non-cancerous tissue Ω_H (including the ECM, healthy cells and any other material immediately surrounding the tumor). The following two cases will be considered: (i) the absence of blood vasculature in D and (ii) a preexisting vasculature in D. The surrounding noncancerous tissue in Ω_H contains a variety of host cells such as fibroblasts, macrophages and blood vessels, all of which have been shown to be important factors in tumorigenesis [56]. However, we have chosen to disregard these aspects of tumor growth to give emphasis on chemotaxis and haptotaxis.

We assume that cell birth and death are in balance in Ω_H and so there is no change in the volume in that region. Let Σ_T denote the boundary of the tumor mass Ω_T. We choose to focus on the key variables involved in tumor cell growth and invasion; nutrient concentration (ρ_N), MDE concentration (ρ_M) ECM density(ρ_E), soluble ECM density(ρ_S), cellular velocity field (u) and solid pressure (p) We derive a system of coupled partial differential equations to model tumor growth in the surrounding tissue and present numerical solutions in two spatial dimensions describing the macroscopic dynamics of invasion in different tumor microenvironments due to haptotaxis and chemotaxis.

2.1 Nutrient Transport

In our model, the net effect of nutrients and growth-promoting and inhibiting factors are described with a single nutrient (oxygen). The nutrient concentration satisfies the advection-diffusion-reaction equation:

$$\nabla \cdot (D_N \nabla \rho_N) = (\delta_N \rho_N) I_{\Omega_T} \tag{1}$$

Here, D_N is the nutrient diffusivity, δ_N is the rate of nutrient uptake by the tumor cells (assumed constant) and I_{Ω_T} is a characteristic function equal to 1 (0) inside (outside) of the tumor region Ω_T . As nutrient diffusion is a much faster process than the cell growth, the nutrient concentration equation can be assumed quasi-steady. Considering the velocities involved in tumor growth [57], the nutrient advection is also negligible compared to diffusion [58]. We assume that tumor cells uptake nutrient at a greater rate than that of noncancerous cells, and so nutrient uptake is negligible in Ω_H [59-61]. Furthermore, we assume that there is little cellular debris in Ω_H and therefore no nutrient decay in that region. The nutrient concentration and flux are assumed to be continuous across the tumor boundary. The two cases that we consider are (i) a low-nutrient environment (e.g., no pre-existing blood vasculature in the computational domain) and (ii) a high-nutrient environment (e.g., the presence of a pre-existing network of nutrient-supplying blood vessels in the domain). For case (ii), nutrient delivery by the blood vasculature and uptake by noncancerous cells are assumed to be in balance outside of Ω_H so that the blood vasculature sufficiently delivers nutrient so that ρ_N is a constant ($\rho_{N\infty}$) at the boundary of the computational domain. So for case (i), we solve Eq. 1 in the entire domain while for case (ii) we solve it only for the tumor region.

2.2 The MDE, Intact ECM and Soluble ECM Density

MDEs are important at many stages of tumor growth, invasion and metastasis, and the manner in which they interact with inhibitors, growth factors and tumor cells is very complex. The ECM is a complex mixture of macro-molecules; but for simplicity, we represent it with a single concentration. Similarly, we characterize MDE and soluble ECM with single concentrations. The production of MDEs and subsequent degradation of the ECM play a role in providing room for the tumor to expand into the surrounding tissue. MDEs are produced (or activated) by the tumor cells at a constant rate λ_M and diffuse throughout the tissue. Removal of MDEs takes place due to natural decay and by deactivation of the enzymes at a constant rate λ_{DM}. The equation governing the evolution of MDE concentration is therefore given by,

$$\frac{\partial \rho_M}{\partial t} = \nabla \cdot (D_M \nabla \rho_M) + \left(\lambda_M (\rho_{M_0} - \rho_M)\right) I_{\Omega_T} - \lambda_{DM} \rho_M \quad . \tag{2}$$

Here, ρ_{M0} is the maximum sustainable concentration of MDE. Experimental work has found that the MDE concentration is kept in check by the opposing anti-proteases secreted by nearby healthy tissue [62]. Therefore following the model in [19], we model this effect with a production term that saturates at the maximum sustainable concentration. Because the coefficient of diffusion of MDE (D_M) is much smaller than that of oxygen, the full time-dependent diffusion equation is used. Following [63], MDE advection term is not included because diffusion time scale (per second) is very shorter than cell growth time scale (per days). The interactions between cancer cells and the surrounding ECM are known to play an important role in carcinogenesis. The intact ECM density is governed by the following equation.

$$\frac{\partial \rho_E}{\partial t} = -\lambda_{DE} \rho_M \rho_E / \rho_{M0} \tag{3}$$

The ECM is considered as non-motile structural matter, so doesn't have advection and changes in its distribution are due to its local degradation by MDEs upon contact, at the rate λ_{DE}. Although the ECM functions directly as a growth restraint for tumor cells, we have not included it in our model in order to investigate the effect of directional migration (via chemotaxis and haptotaxis) on tumor growth and morphology. The ECM may also deform and remodel in response to pressure, proteolysis and to insoluble ECM macro-molecules released by the cells, but we have not considered this. The structure of the ECM has a profound effect on tumor morphology as demonstrated by the model in [64], however in this paper we will consider the ECM as a homogeneous material.

The soluble ECM is produced from the degradation of ECM by MDE at a rate λ_{DE} and diffuses at the rate D_S. The soluble ECM density is given by [1],

$$\frac{\partial \rho_S}{\partial t} = \nabla.(D_S \nabla \rho_S) + \lambda_{DE} \rho_M \rho_E / \rho_{M0} \tag{4}$$

Following [1], soluble ECM advection term is neglected because diffusion time scale (per second) is very shorter than cell growth time scale(per days). We neglect the repeated breakdown of ECM fragments known unlike [1]. In the boundary of the computational domain, we take the boundary conditions $\rho_M = 0$, $\rho_S = 0$ and $\rho_E = \rho_{E\infty}$ (ECM density at far field).

2.3 Cellular Velocity Field

Following previous studies, it is assumed that the tumor is a viscous, inertialess fluid and that all tumor cells move with a single cellular velocity field $\vec{u}$. The tumor boundary moves with the cell velocity at the tumor-host interface. Mathematically, chemotaxis and haptotaxis take the same form as movement of cells is directed towards high concentrations of the substrates. The motion of the cancer cells is governed by the proliferation pressure p and chemotactic and haptotactic response to soluble ECM and intact ECM gradients, respectively.

$$\vec{u} = \mu(-\nabla p + \chi_S \nabla \rho_S + \chi_E \nabla \rho_E) \tag{5}$$

Here, μ is the mobility coefficient and χ_S and χ_E are the chemotaxis and haptotaxis coefficients. We assume that the mobility coefficient (μ) accounts for the environmental effects and measures the overall ability of tumor tissue to respond to the pressure gradients and also characterizes the permeability of the tumor cells. The cell chemotaxis and haptotaxis coefficients are both assumed to be non-negative and constant in Ω_T. Cancer cell motility depends not only on ECM gradients (haptotaxis) but also on ECM density (haptokinesis) as demonstrated by the model in [65]. However, since our focus here is on gradient-driven migration, we effectively choose to ignore the dependence of the cancer cell motion on the ECM density in the absence of ECM gradients. We assume that the normal velocity is continuous across the tumor boundary. The density ρ_T of the tumor tissue in Ω_T obeys the following advection-reaction equation.

$$\frac{\partial \rho_T}{\partial t} + \nabla \cdot (\vec{u} \rho_T) = \lambda_p \rho_T \rho_N / \rho_{N_\infty} - \lambda_A \rho_T \tag{6}$$

In the sharp-interface context, there is a sharp interface between the tumor and host regions [17, 19-21, 28, 48-55]. As mentioned earlier that the total density of tumor cells is constant inside the tumor and drops sharply to zero in the tumor exterior. As cells have a proclivity to remain bound to each other, the constant tumor density ρ_T is also known as close-packing density. We therefore prescribe $\rho_T = 0$ in Ω_H and $\rho_T = 1$ in Ω_T, to obtain

$$\nabla \cdot u = (\lambda_p \rho_N / \rho_{N_\infty} - \lambda_A) I_{\Omega_T} \tag{7}$$

We assume that in the tumor region, cell-mitosis is proportional to the amount of nutrient present and that volume loss due to cellular apoptosis occurs at the rate λ_A. We also assume that there is no proliferation in the host microenvironment. Lastly, the diffusion of tumor cells is an order of magnitude smaller than advection [48] and is therefore neglected.

2.4 Mechanical Pressure

The tumor cells at the continuum level are modeled as a fluid flowing through a porous medium (e.g. the ECM). Primarily, tumor growth depends on the balance between expansive forces caused by cell proliferation and cell-cell adhesion forces, which maintain the tumor's compactness. When there is no taxis, continuity of the normal velocity across the tumor boundary dictates that there is no jump in the normal derivative of p across Σ_T; i.e., $[\mu \delta p/\delta n] = 0$. Assuming uniform cell-cell and cell-matrix adhesion throughout the tumor, the adhesive pressure can be incorporated as a Laplace-Young surface-tension-like jump boundary condition at the tumor-host interface Σ_T: $[p] = p_{outer} - p_{inner} = \Gamma * k$, where k is the mean curvature of the interface and Γ is a constant adhesion parameter analogous to a surface-tension coefficient. Thus, the adhesive forces are modeled by a curvature boundary condition on the interface Σ_T. This representation of adhesion is relatively simple and indirect, however, involving no explicit modelling of cell–cell or cell–ECM contact. In these approaches cell-to-cell and cell-to ECM adhesion are modelled as tumor shape stabilizing mechanical forces which is supported by the experimentally observed presence of surface tension at growing tissue boundaries[66, 67]. The non-cancerous tissue in Ω_H is assumed to be close enough to the tumor to be affected by the pressure changes within the computational domain. The pressure is assumed to satisfy the boundary condition at the computational domain, p = 0; i.e., there is no extra pressure outside the computational domain. The MDE activity is centered almost exclusively within a narrow region adjacent to the tumor surface, as it is kept in check by the opposing anti-proteases secreted by nearby healthy tissue [62]. Similarly we assume that the chemotaxis of gradients of soluble ECM acts only near the interface. Therefore, we take taxis coefficients as piece-wise constant terms i.e., in the tumor region they are positive numbers and outside the tumor, they are set to zero. Thus, the pressure satisfies the following normal jump condition.

$$[\partial p/\partial n] = [\chi_S \, \partial \rho_S/\partial n] + [\chi_E \, \partial \rho_E/\partial n] \tag{8}$$

We define the net pressure responsible for the tumor growth, $p_{net} = p - (\chi_E \rho_E + \chi_S \rho_S)$
So Eq. (5) becomes,

$$\vec{u} = -\mu \nabla p_{net} . \tag{9}$$

By combining Eqs. (7) and (9), we obtain the following governing equation for p_{net} .

$$\mu \nabla^2 p_{net} = \left(-\lambda_p (\rho_N / \rho_{N_\infty}) + \lambda_A\right) I_{\Omega_T} \tag{10}$$

with the following jump conditions on pressure and its normal gradient across the tumor boundary.

$$\left[\mu \partial p_{net}/\partial n\right] = 0, \quad \left[\mu p_{net}\right] = \kappa \Gamma + (\chi_S \rho_S + \chi_E \rho_E)_{\Sigma_T} \tag{11}$$

Once the net pressure is known, we can calculate the cell velocity $\vec{u}$ from Eq. 9. In the rest of the paper we refer net pressure as pressure.

2.5 Nondimensionalization

Before solving the system of governing equations numerically, the parameters and variables are nondimensionalized using the following characteristic scales [19].

$$L \equiv \sqrt{D_N/\delta_N} = 200\,\mu m\,, \quad \tau \equiv \lambda_{P,\max}^{-1} = 1/\,max\,proliferation\,rate = 1.5\,days \tag{12}$$

The length scale L corresponds to the maximum invasion distance at the early stage of tumor invasion. The characteristic tumor pressure $p_T = L^2\lambda_{P,\max}/\mu$ is that which results in maximum cell proliferation with a nondimensional cell speed of unity. As reference densities, we use the far-field nutrient concentration $\rho_{N\infty}$, the intact-ECM density $\rho_{E\infty}$ and the maximum sustainable MDE and soluble-ECM densities ρ_{M0} and ρ_{S0}, respectively. The field variables are made dimensionless as specified in Table 1, while non-dimensional parameters are defined in Table 2. The dimensionless governing equations in terms of the nondimensional variables and parameters defined in Tables 1 and 2 are provided below. We use the same symbols for the non-dimensional variables as those used for the respective dimensional variables defined above.

The dimensionless governing equations can then be written in the following general form:

$$\left.\begin{aligned} \frac{\partial \rho_M}{\partial t} &= \nabla\cdot(D_M\nabla\rho_M) + \left(\lambda_M(1-\rho_M)\right)I_{\Omega_T} - \lambda_{DM}\rho_M \\ \frac{\partial \rho_S}{\partial t} &= \nabla\cdot(D_S\nabla\rho_S) + \lambda_{DE}\rho_M\rho_E \\ \nabla^2\rho_N &= \rho_N I_{\Omega_T}\,, \quad \frac{\partial \rho_E}{\partial t} = -\lambda_{DE}\rho_M\rho_E \\ \nabla^2 p_{net} &= (\lambda_A - \lambda_P\rho_N)I_{\Omega_T}\,, \quad \vec{u} = -\nabla p_{net} \end{aligned}\right\} \tag{13}$$

The following nondimensional initial and boundary conditions are applied.

$$\left.\begin{aligned} \left(\rho_E = 1,\ \ \rho_M = \rho_S = 0\right)_{t=0} \\ \left(\rho_N = \rho_E = 1,\ \ \rho_M = \rho_S = p_{net} = 0\right)_{\Sigma_\infty} \\ \left[\partial p_{net}/\partial n\right] = 0, \quad \left[p_{net}\right] = \kappa\Gamma + \left(\chi_S\rho_S + \chi_E\rho_E\right)_{\Sigma_T} \end{aligned}\right\} \tag{14}$$

The tumor boundary moves with the cell velocities at the tumor-host interface. The haptotactic coefficient =2600 $cm^2/s/M$ was estimated to be in line with that calculated in [68] and the parameter $\rho_{E\infty}$ =10^{-8} - 10^{-12} M is found from [69]. We take $\rho_{E\infty}$=8.42*10^{-7} M. Estimates for the ECM degradation and MDE diffusion, production and degradation coefficients are not available since these are very difficult to obtain experimentally [70]. We have used [19] for these values. According to [1], the MDE and soluble ECM diffuse at the same rate, so we have used to be same as in [19]. Table 2 also has all the references from where we have chosen our parameter values

3. Numerical Method

The set of governing equations, Eqs. (13) and (14), are solved throughout the entire computational domain, on a uniform 2D Cartesian mesh, except for the Poisson equation for ρ_N, which for high- nutrient case is solved for the tumor region Ω_T only. Because we anticipate frequent and complex morphological tumor-surface changes we use the level-set method, based on a reformulation of a model proposed in [22]. Let φ be an auxiliary level-set function whose zero level set denotes the boundary Ω_T of a tumor growing into a surrounding, non-cancerous tissue, satisfying $\varphi < 0$ inside Ω_T, $\varphi > 0$ outside Ω_T, and $\varphi = 0$ on the tumor boundary Σ_T. We update the position of the interface by solving the PDE,

$$\frac{\partial \phi}{\partial t} + \vec{u} \cdot \nabla \phi = 0 \tag{15}$$

We solve Eq. (15) with the semi-Lagrangian scheme developed by Aldredge [71] using upwind transient interpolation modeling [72, 73]. The scheme provides third-order spatial accuracy and shape preservation. We use the immersed interface method [74] to solve for pressure, which is discontinuous across the tumor-host interface, in accordance with the boundary conditions specified above—i.e., Eq.(11). This requires calculation of normal vectors and curvature at the interface using the level-set function. For accurate normal and curvature calculation we reinitilize φ at every time step by solving the following equation [75, 76].

$$\frac{\partial \phi}{\partial \tau} - sign(\phi^0)(1 - |\nabla \phi|) = 0 \tag{16}$$

where φ^0 is the level set function prior to reinitialization and τ is the reinitialization time, reset to 0 at the beginning of each reinitialization process. We discretize the temporal derivative using a third-order total-variation-diminishing Runge-Kutta method (TVD-RK) and approximate $sign(\varphi^0)$ |grad(φ)| with the fifth-order WENO scheme [77]. However when two interfaces are in close contact, level set functions develop singularities that yield inaccurate normal vectors and curvatures when applying traditional discretization methods. In these cases, we construct the level-set function on a local subgrid where we can accurately calculate the normal vectors and curvature using standard discretization methods [18, 78]. As the velocity field near the interface is very sensitive to variations in the curvature, we use a gaussian smoothing filter to damp high frequency pertubations in the speed and interface position, in accordance with [18].

The steps for solving the system of PDEs governing the tumor growth in our model are as follows.

(i) Initialize a level set function φ to represent the interface Σ_T.
(ii) Solve the system of governing equations given in Eq. (13) subject to the initial and boundary conditions in Eq. (14) to obtain $\rho_M, \rho_N, \rho_S, \rho_E$, p_{net} and $\vec{u}$. The Alternating Direction Implicit (ADI) method [79] is used to obtain ρ_M and ρ_S, while ρ_E and p_{net} are obtained using the second-order Runge-Kutta and immersed-interface methods, respectively.
(iii) The velocity field $\vec{u}$ is obtained by using central differences to estimate the pressure gradient. Filter the velocity field using a gaussian smooting filter to remove high frequency noise.
(iv) Set the next overall time step, in accordance with the Courant-Friedrichs-Lewy (CFL) requirement for numerical stability.
(v) Update the position of the boundary $\sum_T$ by solving Eq. (15) for the level-set function φ with the newly obtained velocity field $\vec{u}$.
(vi) Reinitialize φ to maintain it as a signed distance function, by solving Eq. (16)
(vii) Repeat steps (ii)-(vi) for each new time step.

4. Results and Discussion

We investigate the effect of haptotaxis and chemotaxis on tumor growth in a computational domain Ω of size [0, 20] × [0, 20] with grid size 256X256. An initial tumor shape which is slightly elliptical and centered on the domain is prescribed by the following equation.

$$\frac{(x-10)^2}{2.1^2}+\frac{(y-10)^2}{1.9^2}=1 \tag{17}$$

This elliptical tumor's major and minor axes lengths are 840 and 760 μm, respectively (for the length scale L=200 μm). A one-millimeter-radius spheroidal tumor contains around one million cells [41]. The tumor initial shape is elliptical for initiating a small perturbation (to break symmetry) on the tumor size which has been also used as an initial condition by other model. To minimize the influences of the computational-domain boundary, we stop the simulation when the tumor boundary is within 4 distance units of the boundary of the computational domain. We assume that the ECM is initially not degraded (i.e., ECM=1, soluble ECM=0 and MDE=0 in the entire domain) and investigate tumor growth in nutrient-rich and nutrient-poor microenvironments with chemotaxis and haptotaxis. Initial nutrient distribution is not required as Eq. 1 is quasi-steady. To assess tumor growth, we calculate the tumor area and surface perimeter at regular intervals. Following [17], we define the following parameters to characterize the morphological characteristics of the tumor.

Shape parameter: $S = (\text{Perimeter})^2/(4\pi*\text{Area})$
Length Scale: LS=2*Area/Perimeter

The shape parameter S is a measure of the non-circularity of the tumor shape; when S=1, the tumor shape is a circle. The length scale LS is a measure of the smallest dimension of the tumor. For example, for a rectangular tumor with width W and length L, LS = LW/ (L + W) and LS = W if W<<L. For better understanding of these parameters refer to Fig. 2, which shows how S and LS vary with tumor morphology.

4.1 Effect of chemotaxis in a nutrient-poor microenvironment

Earlier studies using hybrid (discrete–continuum) model including haptotaxis [31, 32, 64] demonstrated that a fingered tumor morphologies can be induced by lowering the nutrient concentration (in the microenvironment) even in a homogeneous ECM whereas the tumor is non-invasive for nutrient rich environment. Here, we investigate the influence of soluble ECM as a chemoattractant, in addition to the haptotactic effects, on tumor growth and morphology in a nutrient-poor environment, which has not yet been reported in the literature. According to the work of Perumpannani et al. [1], invasiveness decreases as the chemotactic coefficient is increased. As hypoxia leads to instabilities in tumor growth, the inhibitory effects of soluble ECM gradients during tumor invasion should be investigated along with hypoxia and haptotaxis subject to variations in the magnitude of the chemotaxis coefficient.

We consider a tumor with an initial shape defined by Eq. 17 growing in a low-nutrient environment. Relevant baseline parameter values are listed in Table 2. Table 3 shows the values used for parameter sensitivity studies. In order to understand the effect of chemotaxis on tumor growth and morphology, we first compare the cases of no taxis (no directed cell motion) and haptotaxis only and chemotaxis only. The morphological evolution of the tumor in the computational domain with time are shown in Fig. 2 for the cases of no taxis (Fig. 2a-b), haptotaxis only (with coefficient χ_E=1) (Fig. 2c-e) and chemotaxis only (with coefficient χ_S=10) (Fig. 2f-g). The ECM gradients near the boundary of the tumor are responsible for the motion of the tumor cells via haptotaxis. The tumor develops four large, symmetric bulbs with very narrow necks (Fig. 2e), which continue to spread in the computational domain and eventually split into four pieces.

If we consider chemotaxis only (with χ_S=10), the tumor stops growing after a certain time and the morphology is stable, i.e. circular (Fig. 2g). So the instability due to the perturbed initial tumor shape does not grow in spite of hypoxia, due to the inhibitory effect of chemotaxis.

The combined effects of chemotaxis and haptotaxis on tumor morphology are shown in Fig. 3 for χ_E=1 and χ_S=10. The contours of MDE, ECM and soluble ECM at different times are shown in Fig. 4. Both MDE and soluble ECM are diffusible, so we notice smooth contours unlike for ECM contours. Soluble ECM is made from ECM upon degradation, so where ECM is the lowest, soluble ECM is the greatest. During earlier times the tumor elongates along the y-axis and bulges are formed along left and right sides, which continue to grow deeper with increasing time. We notice that while the initial tumor shape perturbation is along x-axis, the tumor-surface instability grows along the y-axis due to the combined effects of chemotaxis and haptotaxis. This is due to the fact that during early times the ECM gradients are greatest on the left and right sides of the tumor, which causes the soluble ECM gradients to be greatest in these regions. The chemotactic influence prevents tumor growth due to cell proliferation and haptotaxis in these regions, while the top and bottom surfaces grow. The net effect is tumor elongation along y-axis. The growth of the left and right bulges can be explained by the plots of gradients of ECM and soluble ECM in Fig. 5. As soluble ECM is diffusible, its gradients are smaller (as seen in Fig. 5a) than the gradients of ECM (Fig. 5b) in the computational domain. The net gradients of ECM and soluble ECM (similar to Fig. 5b qualitatively) causes the growth of the left and right bulges and the formation of the two symmetric buds. The gradients in regions near the top and bottom tumor surfaces are smaller and uniform (not shown here) which promote slow and uniform growth on these regions.

So for combined effects of haptotaxis and chemotaxis, the tumor morphology is still unstable and different from that with only haptotaxis considered (Fig. 2c-e). We can conclude, therefore, that for these extents of chemotaxis and haptotaxis, the instability due to cell-proliferation and haptotactic attraction of ECM gradients is not counteracted by the chemotactic attraction of soluble ECM gradients. The influence of the extent of chemotaxis on tumor shape and growth and morphology is shown in Fig. 6 and Fig.7 respectively using different values of chemotaxis coefficients listed in Table 3. If we increase the chemotaxis coefficient fivefold (i.e., χ_S=50 and χ_E=1), the tumor growth further slows and the bulbs are formed later (compared to the growth with χ_S=10 and χ_E=1), after the tumor has elongated vertically to a greater extent. However, for both values of the chemotaxis coefficient considered, tumor growth is unstable and a thin neck forms which may split into two symmetric buds. The tumor growth is stable when we increase the chemotaxis coefficient tenfold (i.e., χ_S=100 and χ_E=1). As is evident in the plots of tumor area and perimeter versus time (Fig.7a and 7b, respectively), chemotaxis slows tumor growth and for χ_S=10, χ_E=0 and for χ_E=1, χ_S=100 tumor growth stops after a certain time when cell motion due to proliferation and haptotaxis are balanced by the chemotactic motion.

We can gain a more detailed understanding of the invasion process resulting from the combined effects of chemotaxis and haptotaxis by examining the evolution of the shape parameter S and length scale LS, plotted in Figs. 7c and 7d, respectively. Initially, S is constant and nearly unity as a result of uniform tumor growth, while LS increases with increasing tumor size. Later, S steadily rises as the tumor elongates, becomes increasingly noncircular and forms bulges for both χ_E=1 (with χ_S=0) and with combined effects of haptotaxis and chemotaxis (with χ_E=1 and χ_S=10 and 50). The LS concomitantly decreases, since the width of the tumor decreases as the tumor elongates. For both χ_S=10 (with χ_E=0) and χ_S=100 (with χ_E=1), shape parameters (Fig. 7c) are always near unity which indicates stable growth even there is initial shape instability, while length scales (Fig. 7d) eventually become relatively constant with increasing time.

Thus, considering only chemotaxis can result in stable tumor growth in nutrient-poor microenvironments. When the effects of haptotaxis are considered, we find that chemotaxis inhibits tumor growth and changes the overall growth response of the tumor. However, the stability of tumor morphology strongly depends on the extent of chemotaxis.

4.2 Effect of chemotaxis in a nutrient-rich microenvironment

Previous studies report that the tumor growth is compact (non-invasive) in nutrient-rich environments and even haptotaxis has no distinct effect on morphology [32]. Here, we investigate the effects of chemotaxis for tumors growing in high-nutrient environments, not previously addressed in the literature. This case applies to a tumor with an adequate supply of nutrient from either pre-existing or newly developed vasculature through angiogenesis. As angiogenesis inhibitors are used with the intent of halting or slowing tumor growth, the inhibitory effects of soluble ECM gradients during tumor invasion should be investigated subject to variations in the value of the chemotaxis coefficient, considering haptotaxis and an adequate supply of nutrients in the tumor microenvironment.

First, we consider the case when there is only haptotaxis-induced cell movement (with χ_E=1) and tumor growth depends on cell proliferation and haptotaxis. Relevant values for baseline parameters and parameter sensitivity studies are given in Tables 2 and 3, respectively. The evolution of the tumor morphology with time is displayed in Fig. 8a-d for this case in which the nutrient concentration is always maximum (ρ_N=1) on the tumor boundary (as shown in Fig. 8e). The increased nutrient supply in this case increases proliferation and, in turn, causes large solid pressures (cf. Fig. 8f) to form in the proliferating region, which cause the tumor to grow even more rapidly, further enhancing this effect. The tumor develops an H-shaped structure in this case. The morphologies here are very similar to those for the case without taxis, as described in [48], although the tumor grows faster due to the combined effect of cell proliferation and haptotaxis. If we consider chemotaxis only (with χ_S=10), the tumor morphology is not stable (similar to that shown in Fig. 8), unlike for the case of growth in a nutrient-poor microenvironment. The dual influence of chemotaxis and haptotaxis on tumor morphology for χ_E=1 and χ_S=10 is also similar to that suggested in Fig. 8.

Fig. 9 shows the evolution of tumor morphology with a fivefold increase in the chemotaxis coefficient (i.e., χ_E=1 and χ_S=50). We observe that while the initial perturbation is along x-axis, the tumor surface instability grows along the y-axis due to the combined effect of chemotaxis and haptotaxis. During early times, these morphologies are similar to those shown in Fig. 3 for tumor growth in a nutrient-poor microenvironment due to the combined effects of chemotaxis and haptotaxis with χ_E=1 and χ_S=10. Left and right bulges are formed while the surfaces near the top and bottom of the tumor continue to bend inward without reconnecting, growing bigger and spreading throughout the computational domain. Similar morphologies are observed with a tenfold increase in the chemotaxis coefficient (i.e. χ_E=1 and χ_S=100), although with slower rates of growth. If the chemotaxis coefficient is further increased, by a factor of fifty (i.e., χ_E=1 and χ_S=500), stable growth is achieved. For different values of chemotaxis coefficients (listed in Table 3) the tumor morphologies and the growth dynamics are shown in Fig. 10 and Fig. 11, respectively.

We notice that during early times the tumor area, perimeter and shape parameter all are nearly similar in Fig.11a-c. This is due to the fact that the large solid pressure caused by the faster proliferation in the nutrient-rich microenvironment is substantially greater than the change in solid pressure due to chemotaxis and haptotaxis. Later on, the influence of chemotaxis alone and the combined influence of chemotaxis and haptotaxis become evident in the results plotted as the tumor area, perimeter and shape parameter increase with time. With increasing extent of chemotaxis, tumor growth slows, but does not become stable. Thus, our simulations of tumor growth in nutrient-poor and nutrient-rich environments clearly show that chemotaxis can inhibit tumor growth irrespective of the level of nutrient concentration in the microenvironment, and the stability depends on the extent of chemotaxis. However, the effect of chemotaxis is more pronounced for tumor growth in nutrient-poor microenvironments.

4.3 Effect of biophysical parameters in nutrient-poor and nutrient-rich microenvironments

Parameter sensitivity studies for haptotaxis show that variations of the MDE diffusion coefficient D_M, ECM degradation rate λ_{DE}, MDE production rate λ_M and MDE decay rate λ_{DM} change tumor growth greatly [70, 80]. The chemotaxis-haptotaxis model in [1] investigated the effects of varying ECM degradation rate

λ_{DE} and MDE production rate λ_M in one spatial dimension and predicted that the tumor invasiveness will first increase with increase in λ_{DE} and/or $\lambda_{M,}$ but then decrease for excessive increase in λ_{DE} and/or λ_M. We will investigate the influence of various biophysical parameters related to soluble ECM production on tumor growth and morphology using our chemotaxis-haptotaxis model, accounting for variations in nutrient concentration, which has not been previously reported in the literature. In particular, we consider the effect of varying the ECM degradation rate, λ_{DE} and the MDE production rate $\lambda_{M,}$ on the morphology of tumors growing in nutrient-poor and nutrient-rich microenvironments using the baseline values in Table 2.

We consider increases in the value of λ_{DE} by factors of 10 and 100 (i.e. λ_{DE} =0 .10 and λ_{DE}=1.0, respectively), representing increased ECM degradation and concomitant increased production of soluble ECM. The tumor growth under the combined influences of haptotaxis and chemotaxis (i.e., χ_E=1 and χ_S=10) is unstable (as shown in Fig. 3). The resulting tumor shapes due to the effects of increasing λ_{DE} are displayed in Fig. 12 for both low and high nutrient environments. It is clear that as λ_{DE} increases, the tumor elongates more vertically for the low-nutrient case. For the nutrient-rich case, tumor morphologies also change (more vertical elongation which means more invasion into the host tissue) with increasing λ_{DE}. If we increase λ_{DE} further, i.e., λ_{DE} =10, the tumor growth slows down. Although the shapes that evolve in these two environments are qualitatively different, there are shape instabilities in each case that are not fully damped due to increased soluble ECM production resulting from increased ECM degradation.

Fig. 13 demonstrates the effect of increasing λ_{DE} on tumor growth dynamics and morphology with time. For both environments, the instability develops earlier with increasing λ_{DE}, although the slopes of the curves increase greatly with increasing λ_{DE} for low-nutrient environments. This is because the gradients of ECM and soluble ECM both increase as λ_{DE} increases. As soluble ECM gradients will inhibit growth, and ECM gradients will accelerate growth, faster growth indicates that the effects of haptotaxis become stronger with increasing λ_{DE} for tumor growth in both environments. Most importantly, for very large rate of λ_{DE} (=10) we see that the growth rate again slows down for both environments. To support this fact, we tabulate the time at which tumor shape parameter is 1.5 with increasing λ_{DE} by an order of magnitude in Table 4. So, our model predicts an increase in invasiveness with increase in λ_{DE} and decrease in invasiveness at very high levels of ECM degradation for both microenvironments. More importantly, although showing biphasic growth responses with increase in λ_{DE}, the tumor growth is still unstable for this extent of chemotaxis.

Next, we consider the effect of increasing MDE production. If MDE is produced at a greater rate, ECM will be degraded more rapidly while fragments of ECM production will increase. Thus, greater MDE production also favors both haptotaxis and chemotaxis. Fig. 14 shows the resulting tumor shapes as λ_M is increased from 10 to 1000 (in increments of 10). Tumor shapes change greatly with increasing λ_M for the low-nutrient case, while remaining unchanged for the nutrient-rich case. The effects on tumor growth and morphology with time are shown in Fig. 15, where it is clear that the tumor develops instability faster for both environments with increasing λ_M. Table 5 shows the time at which tumor shape parameter is 1.5 for increasing λ_M, which also supports this fact. However, the slopes of the curves remain essentially unchanged with increasing λ_M for nutrient-rich tumor growth and decrease (except for area vs. time in Fig 15a) with increasing λ_M for the case of nutrient-poor tumor growth. This indicates that increasing λ_M has a greater influence in the nutrient-poor case, in terms of both tumor growth and morphology. Faster growth with increasing λ_M means that the effect of haptotaxis is greater than that of chemotaxis.

Our chemotaxis-haptotaxis model therefore predicts that increasing λ_{DE} and $\lambda_{M,}$ change the overall growth response of the tumor irrespective of the nutrient concentration in the tumor microenvironment. Furthermore for all values of λ_{DE} and λ_M, the tumor morphologies are unstable with χ_E=1 and χ_S=10. Although increase in λ_{DE} shows the biphasic tumor growth response for both environments as predicted in [1], the stability depends on the strength of chemotaxis. Decreasing the MDE production rate increases the chemotactic influence irrespective of the concentration of nutrient in the tumor microenvironment.

4.4 Chemotaxis and surface-tension in a nutrient-poor microenvironment

Tumor cells tend to adhere less to their neighbors [81] and must lose their adhesion to other cells to enable malignant invasion [82]. Cell-cell adhesion mediated with E-cadherin (a calcium-regulated adhesion molecule expressed in most normal epithelial tissues) prevents invasiveness of cancer cells [83]. For nutrient-poor tumor growth, increasing adhesion can limit the rate of tumor fragmentation and the extent of tissue invasion [17]. Morphological instabilities were observed for nutrient-poor tumor growth, with the degree of instability increasing greatly with decreasing surface tension [23]. The fingering tumor cell population generally have low cell adhesion and oxygen consumption rates [32] and are observed for a combination of the strength of cell-cell adhesion and haptotaxis [33]. We demonstrate in section 4.1 that chemotaxis due to the gradients of soluble ECM can prevent tumor shape instabilities developed due to hypoxia and haptotaxis. In this section, we investigate the effect of surface tension and chemotaxis, in addition to haptotactic effects on tumor growth and morphology in nutrient-poor environments using the values listed in Tables 2 and 6.

If we consider chemotaxis only (with χ_S=10), the tumor stops growing after a certain time and the morphology is stable for both medium and low surface tension ((Γ =0.05 and Γ =0.01, respectively). Thus, in the absence of haptotaxis, instability of the initially perturbed tumor shape is suppressed, despite the hypoxic and low-adhesion microenvironment conditions due to the inhibitory effect of chemotaxis. Next, we investigate the dual effects of haptotaxis and chemotaxis subject to variations of the chemotaxis coefficient. The tumor morphological evolution for the low surface-tension coefficient accounting for the combined influence of chemotaxis and haptotaxis (χ_E=1 and χ_S=10) is shown in Fig. 16. The tumor develops four large, symmetric bulbs with very narrow necks (Fig. 16c), which continue to spread in the domain and eventually split into four pieces. Qualitatively, these morphologies are very similar with haptotaxis (χ_E=1) but no chemotaxis and with medium surface-tension (cf. Fig. 2c-e)

The combined effects of chemotaxis and haptotaxis (for χ_S=50 and χ_E=1) on tumor morphology at different times are as shown in Fig. 17. Increased growth inhibition due to chemotaxis forces the tumor to grow more slowly. During earlier times the tumor elongates along the y-axis and bulges are formed along left and right sides, which continue to grow larger with increasing time. The influence of the extent of chemotaxis on tumor growth and morphology is shown in Fig. 18 for different values of surface tension. The tumor morphologies are unstable for both values of the chemotaxis coefficients (χ_S=10 and χ_S=50) and surface-tension coefficients considered, a thin neck forms; the neck may eventually break, splitting the tumor into symmetric buds. Therefore for these extents of chemotaxis and haptotaxis, the instability due to cell-proliferation and haptotactic attraction is not fully countered by the chemotactic attraction of soluble ECM gradients, even with a fivefold increase in surface tension. We notice that the tumor morphologies are very similar for both surface tension coefficients when χ_S=50 and χ_E=1. The morphologies are stable when we increase the chemotaxis coefficient tenfold (i.e., χ_S=100 and χ_E=1) which is also observed for medium surface tension. So the effect of surface tension decreases as we increase the extent of chemotaxis.

Thus, considering only chemotaxis can result in stable tumor growth in nutrient-poor microenvironments irrespective of the level of adhesion. When effects of haptotaxis are considered, we find that chemotaxis inhibits tumor growth and changes the overall growth response of the tumor, as a result of haptotaxis and the loss of cell-adhesion. Moreover, by increasing the extent of chemotaxis tumor growth can be controlled (stabilized) in low-adhesion conditions; and as the coefficient of chemotaxis increases the influence of cell-adhesion on tumor growth and morphology decreases and becomes eventually negligible (stable growth).

4.5 Effect of chemotaxis in a low-proliferation microenvironment

Tumor cells undergo a variety of biophysical responses in hypoxic conditions, including activation of signaling pathways that regulate proliferation, death, angiogenesis and invasion. Therefore hypoxia is associated with poor prognosis and resistance to radiation therapy [84]. Rapidly growing tumors invariably

contain hypoxic regions. Adaptive response to hypoxia may lead to low cell proliferation. Chemotaxis of tumor cells up nutrient gradients produces branched invasive structures in conditions of low cell proliferation [30] in hypoxic and low-proliferation environments. Thus, it is important to study the effects of chemotactic inhibitory influences on tumor growth and morphology in hypoxic environments for the case of low mitosis rate. Here, we examine the influence of chemotaxis on the dynamics and morphology of tumors for this case, not previously addressed in the literature.

First, we consider the case when there is only haptotaxis-induced cell movement and tumor growth depends on cell proliferation and haptotaxis. Relevant parameters values are given in Tables 2 and 7. The tumor growth is unbounded but circular (i.e., stable) despite haptotaxis (with χ_E=1) due to low cell proliferation. Next, we consider the combined effect of chemotaxis and haptotaxis. The evolution of the tumor morphology with time is displayed in Fig. 19 for χ_E=1 and χ_S=10. We observe that while the initial perturbation is along x axis, the tumor surface instability grows along the y axis due to the combined effect of chemotaxis and haptotaxis. During early times, these morphologies are similar to those shown in Fig. 3 for tumor growth in a nutrient-poor environment due to the combined effects of chemotaxis and haptotaxis, with χ_E=1 and χ_S=10. A possible cause is provided in sect. 4.1. The major difference from sect. 4.1 is that in this case tumor shape is stable for haptotaxis only and there is unstable shrinkage when combined effects are considered. So our model demonstrates that chemotaxis in low mitosis environments can lead to the development of instability, although the chemotactic pull works in the opposite direction of that of invasion.

Fig. 20 shows the growth dynamics of the tumor for different chemotaxis coefficients. We notice that the tumor starts growing (unstable as S>1 in Fig. 20c) for χ_E=1 and χ_S=10 after initial shrinkage whereas with a fivefold and ten-fold increases in the chemotaxis coefficient, the tumor shrinks with time and this shrinkage is stable (S~1 as depicted in Fig. 20c). This is also true for the case of chemotaxis only. However for this range of chemotaxis coefficients, length scale always decreases with time (cf. Fig. 20d). Both stable and unstable shrinkage were predicted in [28] without considering any taxis rather considering the relative rate of mitosis to the relaxation mechanisms (cell mobility and cell-cell adhesion) and the ratio of apoptosis to mitosis with low, moderate and high vascularization. Our model predicts a biphasic response of the tumor in terms of stability with increase in chemotaxis coefficient when haptotaxis alone does not lead to instability. For both low and high values of chemotaxis coefficients the growth is stable and for medium values it is unstable. Therefore, chemotaxis has a stronger influence in low-proliferation environments.

We now consider an increase in the strength of haptotaxis. If we increase the haptotaxis coefficient five-fold (i.e., χ_E=5) and take a chemotaxis coefficient χ_S=10, the morphologies shown in Fig. 21 are obtained, which are very similar to those obtained for the case of haptotaxis only, with χ_E=5. If we consider chemotaxis only (with χ_S=10), the tumor morphology is stable. The dual influence of chemotaxis and haptotaxis on tumor morphology for χ_E=5 and χ_S=50 is also similar to that suggested in Fig. 21. The tumor morphologies and growth dynamics obtained for different values of taxis coefficients are shown in Fig. 22 and Fig. 23, respectively. We notice from Fig. 23 that during early times the tumor starts shrinking due to chemotactic movements, but later becomes unstable (S>1in Fig. 23c) for χ_S=50. This is due to the fact that the instability caused by haptotaxis is not completely damped out by chemotaxis. For χ_S=100 (with χ_E=5) and χ_S=10 (with χ_E=0) there is stable (as S~1 in Fig. 23c) tumor shrinkage. With an increasing extent of chemotaxis, the tumor area, perimeter and length scale all decreases with time.

In summary, our simulations of tumor growth in nutrient-poor and low-proliferation environments clearly show that chemotaxis can inhibit tumor growth, although stability in all cases is not achieved. The tumor shows biphasic stability response due to chemotaxis and may act as a growth destabilizing factor when the haptotaxis alone does not lead to instability. Both stable and unstable shrinkage are possible depending on the strength of chemotaxis. Therefore, anticancer therapies utilizing chemotaxis for low proliferation environment should be designed carefully.

5. Conclusion

To better target MMPs for cancer treatment, an appreciation of their many, often competing influences on cancer progression is needed. Most of the literature supports the notion that the sum of MMP action promotes cancer progression, however the actions of the MMPs that negatively regulate cancer progression have received relatively little appreciation. We have proposed a two-dimensional continuum model for the growth and invasion of tumor cells into healthy tissue that focuses on four key components implicated in the invasion process: tumor cells, intact ECM, MDE, soluble ECM and nutrient, which are initially homogeneous in the tumor microenvironment. The directed cell motions due to chemotaxis and haptotaxis are systematically modeled (along with cell motion due to cell proliferation and adhesion through a curvature boundary condition at the tumor interface), and the motility-retarding effects of soluble ECM by chemotaxis on the tumor-invasion process have been investigated. The extents of chemotaxis, degradation/production of ECM/soluble ECM by MDE and the production rate of MDE are investigated as critical factors in the invasion process.

Tumor growth, morphology and invasion are substantially characterized by whether the tumor is growing in a nutrient-rich or nutrient-poor microenvironment. Our simulation results show that the stable morphologies can be found in both microenvironments for stronger chemotactic movement, although the values of the chemotaxis coefficient required for stabilizing nutrient-rich tumor growth are greater. Although increasing the MDE production and ECM degradation rates changes the overall growth response of the tumor, these rate do not significantly affect stability. Moreover, increasing MDE production rate strengthen haptotactic movement more than that of chemotaxis. There is an optimum ECM degradation rate that results in maximum growth in both environments, but stability is not obvious unless the chemotaxis coefficient is increased.

Previous studies have linked low oxygen levels and loss of adhesion in tumor cells as a contributing factors in the development cancer. So the motility-retarding effects of soluble ECM by chemotaxis on the tumor-invasion process are then investigated for low cell adhesion and low proliferation in a hypoxic environment. When chemotaxis of soluble ECM gradients is included, the effect of adhesion on the tumor shape largely depends on the extent of chemotaxis. In the case of low cell-proliferation, chemotaxis has greater influence, and the tumor may shrink in shape with increasing chemotaxis, an effect not observed for cases of greater cell proliferation. Both stable and unstable shrinkage and biphasic response in terms of stability are predicted by our model. More importantly, in some cases chemotaxis can result in early onset of instability where the tumor growth induced by haptotaxis alone is stable. Thus, combining anti-protease therapy with haptotactic blockade to treat cancer as suggested in [1] should be conducted carefully in low-cell-proliferation conditions.

While there are extensive researches on the prohibiting effects of MMP (by creating structural gradients of insoluble ECM and associated haptotactic motion) on tumor growth and morphology; our model is the first to investigate the inhibitory effects of MMP (by chemotaxis due to soluble ECM gradients) with variations in nutrient availability in the tumor microenvironment. We have also investigated the influence of chemotaxis due to soluble-ECM gradients, for tumors growing in hypoxic environments with varying extents of cell adhesion and cell proliferation rates which was not reported before. These new insights into the growth-inhibiting influence of fragments of ECM through chemotaxis will have important implications on the understanding of tumor-invasion processes and, most importantly, on the development of promising anti-cancer therapeutics. So, the results of our study are useful in advancing our understanding of how the microenvironment may affect tumor invasion at the macroscopic scale and thus will be helpful in the design of cancer therapy.

Most forms of invasive cancers are resistant to the traditional chemotherapy focusing on cytotoxic drugs for killing cancer cells and metastasis is responsible for 90% of patient deaths [85] despite recent advances in drug delivery methods. Although there has been huge amount of evidence implicating the critical roles of MMPs in various stages of cancer growth and progression, we still do not thoroughly understand the critical roles of MMPs in the complex cancer microenvironment, as evidenced by the clinical failure

of first generation MMPIs in phase III trials [86] despite preclinical data indicating that MMPIs have great potential for therapeutic use. As we discussed, the interaction between tumor and its microenvironment plays the crucial role during tumor-invasion processes, therefore, further studies should be carried out to understand comprehensive MMP roles that correlate with cancer progression or drug responses, which is crucial for the clinical development of MMPIs and other cancer therapies. Our study will help cancer researchers to design experimental studies to more closely mimic in vivo scenarios for understanding the accurate knowledge of functions of MMPs. Therefore, the results of our study will bring new light to the field of clinical trials so that pharmaceutical companies will begin investing in a MMP inhibitor program.

References

[1] A.J. Perumpanani, D.L. Simmons, A.J.H. Gearing, K.M. Miller, G. Ward, J. Norbury, M. Schneemann, J.A. Sherratt, Extracellular matrix-mediated chemotaxis can impede cell migration, Proceedings of the Royal Society B-Biological Sciences 265(1413) (1998) 2347-2352.

[2] D.A. Lauffenburger, A.F. Horwitz, Cell migration: a physically integrated molecular process, Cell 84(3) (1996) 359-369.

[3] P. Friedl, K. Wolf, Tumour-cell invasion and migration: diversity and escape mechanisms, Nature Reviews Cancer 3(5) (2003) 362-374.

[4] J.D. Mott, Z. Werb, Regulation of matrix biology by matrix metalloproteinases, Current opinion in cell biology 16(5) (2004) 558-564.

[5] S. Ulisse, E. Baldini, S. Sorrenti, M. D'Armiento, The urokinase plasminogen activator system: a target for anti-cancer therapy, Current cancer drug targets 9(1) (2009) 32-71.

[6] M. Egeblad, Z. Werb, New functions for the matrix metalloproteinases in cancer progression, Nature reviews. Cancer 2(3) (2002) 161-74.

[7] C.M. Overall, O. Kleifeld, Validating matrix metalloproteinases as drug targets and anti-targets for cancer therapy, Nature Reviews Cancer 6(3) (2006) 227-239.

[8] J. Decock, S. Thirkettle, L. Wagstaff, D.R. Edwards, Matrix metalloproteinases: protective roles in cancer, Journal of cellular and molecular medicine 15(6) (2011) 1254-1265.

[9] D. Stellas, E. Patsavoudi, Inhibiting matrix metalloproteinases, an old story with new potentials for cancer treatment, Anti-Cancer Agents in Medicinal Chemistry (Formerly Current Medicinal Chemistry-Anti-Cancer Agents) 12(7) (2012) 707-717.

[10] N.E. Sounni, A. Noel, Targeting the tumor microenvironment for cancer therapy, Clinical chemistry 59(1) (2013) 85-93.

[11] L.A. Liotta, Tumor invasion and metastases--role of the extracellular matrix: Rhoads Memorial Award lecture, Cancer research 46(1) (1986) 1-7.

[12] S. Aznavoorian, M.L. Stracke, H. Krutzsch, E. Schiffmann, L.A. Liotta, Signal transduction for chemotaxis and haptotaxis by matrix molecules in tumor cells, Journal of Cell Biology 110(4) (1990) 1427-38.

[13] J. Klominek, K.H. Robert, K.G. Sundqvist, Chemotaxis and haptotaxis of human malignant mesothelioma cells: effects of fibronectin, laminin, type IV collagen, and an autocrine motility factor-like substance, Cancer research 53(18) (1993) 4376-82.

[14] C. Gialeli, A.D. Theocharis, N.K. Karamanos, Roles of matrix metalloproteinases in cancer progression and their pharmacological targeting, FEBS Journal 278(1) (2011) 16-27.

[15] A. Noel, A. Gutierrez-Fernandez, N.E. Sounni, N. Behrendt, E. Maquoi, I.K. Lund, S. Cal, G. Hoyer-Hansen, C. Lopez-Otin, New and paradoxical roles of matrix metalloproteinases in the tumor microenvironment, Frontiers in pharmacology 3 (2012) 140.

[16] K. Kessenbrock, V. Plaks, Z. Werb, Matrix metalloproteinases: regulators of the tumor microenvironment, Cell 141(1) (2010) 52-67.
[17] P. Macklin, J. Lowengrub, Nonlinear simulation of the effect of microenvironment on tumor growth, Journal of theoretical biology 245(4) (2007) 677-704.
[18] P. Macklin, J. Lowengrub, Evolving interfaces via gradients of geometry-dependent interior Poisson problems: application to tumor growth, Journal of Computational Physics 203(1) (2005) 191-220.
[19] P. Macklin, S. McDougall, A.R. Anderson, M.A. Chaplain, V. Cristini, J. Lowengrub, Multiscale modelling and nonlinear simulation of vascular tumour growth, J Math Biol 58(4-5) (2009) 765-98.
[20] V. Cristini, Morphologic Instability and Cancer Invasion, Clin Cancer Res 11(19) (2005) 6772-6779.
[21] H.B. Frieboes, X. Zheng, C.H. Sun, B. Tromberg, R. Gatenby, V. Cristini, An integrated computational/experimental model of tumor invasion, Cancer research 66(3) (2006) 1597-1604.
[22] C.S. Hogea, B.T. Murray, J.A. Sethian, Simulating complex tumor dynamics from avascular to vascular growth using a general level-set method, Journal of Mathematical Biology 53(1) (2006) 86-134.
[23] N.J. Poplawski, U. Agero, J.S. Gens, M. Swat, J.A. Glazier, A.R. Anderson, Front instabilities and invasiveness of simulated avascular tumors, Bulletin of math biology 71(5) (2009) 1189-227.
[24] N.J. Poplawski, A. Shirinifard, U. Agero, J.S. Gens, M. Swat, J.A. Glazier, Front instabilities and invasiveness of simulated 3D avascular tumors, PloS one 5(5) (2010).
[25] S. Pennacchietti, P. Michieli, M. Galluzzo, M. Mazzone, S. Giordano, P.M. Comoglio, Hypoxia promotes invasive growth by transcriptional activation of the met protooncogene, Cancer Cell 3(4) (2003) 347-61.
[26] J.T. Erler, K.L. Bennewith, M. Nicolau, N. Dornhofer, C. Kong, Q.T. Le, J.T.A. Chi, S.S. Jeffrey, A.J. Giaccia, Lysyl oxidase is essential for hypoxia-induced metastasis, Nature 440(7088) (2006) 1222-1226.
[27] O. Casanovas, D.J. Hicklin, G. Bergers, D. Hanahan, Drug resistance by evasion of antiangiogenic targeting of VEGF signaling in late-stage pancreatic islet tumors, Cancer cell 8(4) (2005) 299-309.
[28] V. Cristini, J. Lowengrub, Q. Nie, Nonlinear simulation of tumor growth, Journal of mathematical biology 46(3) (2003) 191-224.
[29] T. Alarcon, H.M. Byrne, P.K. Maini, A cellular automaton model for tumour growth in inhomogeneous environment, Journal of theoretical biology 225(2) (2003) 257-274.
[30] V. Cristini, X. Li, J.S. Lowengrub, S.M. Wise, Nonlinear simulations of solid tumor growth using a mixture model: invasion and branching, Journal of mathematical biology 58(4-5) (2008) 723-763.
[31] A.R.A. Anderson, A.M. Weaver, P.T. Cummings, V. Quaranta, Tumor Morphology and Phenotypic Evolution Driven by Selective Pressure from the Microenvironment, Cell 127(5) (2006) 905-915.
[32] A.R. Anderson, K.A. Rejniak, P. Gerlee, V. Quaranta, Microenvironment driven invasion: a multiscale multimodel investigation, Journal of mathematical biology 58(4-5) (2009) 579-624.
[33] J. Jeon, V. Quaranta, P.T. Cummings, An off-lattice hybrid discrete-continuum model of tumor growth and invasion, Biophysical journal 98(1) (2010) 37-47.
[34] S. Turner, J.A. Sherratt, Intercellular adhesion and cancer invasion: a discrete simulation using the extended Potts model, Journal of theoretical biology 216(1) (2002) 85-100.
[35] M. Scianna, L. Preziosi, A hybrid model describing different morphologies of tumor invasion fronts, Mathematical Modelling of Natural Phenomena 7(01) (2012) 78-104.
[36] F. Alexis, E.M. Pridgen, R. Langer, O.C. Farokhzad, Nanoparticle technologies for cancer therapy, Drug delivery, Springer2010, pp. 55-86.
[37] J. Pascal, C.E. Ashley, Z. Wang, T.A. Brocato, J.D. Butner, E.C. Carnes, E.J. Koay, C.J. Brinker, V. Cristini, Mechanistic modeling identifies drug-uptake history as predictor of tumor drug resistance and nano-carrier-mediated response, ACS nano 7(12) (2013) 11174-11182.
[38] Z. Wang, R. Kerketta, Y.-L. Chuang, P. Dogra, J.D. Butner, T.A. Brocato, A. Day, R. Xu, H. Shen, E. Simbawa, Theory and experimental validation of a spatio-temporal model of chemotherapy transport to enhance tumor cell kill, PLoS computational biology 12(6) (2016) e1004969.

[39] H.B. Frieboes, B.R. Smith, Z. Wang, M. Kotsuma, K. Ito, A. Day, B. Cahill, C. Flinders, S.M. Mumenthaler, P. Mallick, Predictive modeling of drug response in non-hodgkin's lymphoma, PloS one 10(6) (2015) e0129433.
[40] E.J. Koay, M.J. Truty, V. Cristini, R.M. Thomas, R. Chen, D. Chatterjee, Y.a. Kang, P.R. Bhosale, E.P. Tamm, C.H. Crane, Transport properties of pancreatic cancer describe gemcitabine delivery and response, The Journal of clinical investigation 124(4) (2014) 1525.
[41] J. Pascal, E.L. Bearer, Z. Wang, E.J. Koay, S.A. Curley, V. Cristini, Mechanistic patient-specific predictive correlation of tumor drug response with microenvironment and perfusion measurements, Proceedings of the National Academy of Sciences of the United States of America 110(35) (2013) 14266-71.
[42] A.J. Perumpanani, H.M. Byrne, Extracellular matrix concentration exerts selection pressure on invasive cells, European journal of cancer 35(8) (1999) 1274-80.
[43] H. Berry, V. Larreta-Garde, Oscillatory behavior of a simple kinetic model for proteolysis during cell invasion, Biophysical journal 77(2) (1999) 655-665.
[44] V. Larreta-Garde, H. Berry, Modeling extracellular matrix degradation balance with proteinase/transglutaminase cycle, Journal of theoretical biology 217(1) (2002) 105-124.
[45] A. Häcker, A mathematical model for mesenchymal and chemosensitive cell dynamics, Journal of mathematical biology 64(1-2) (2012) 361-401.
[46] H.B. Frieboes, J.S. Lowengrub, S. Wise, X. Zheng, P. Macklin, E.L. Bearer, V. Cristini, Computer simulation of glioma growth and morphology, NeuroImage 37 (2007) S59-S70.
[47] H.M. Byrne, M.A.J. Chaplain, Modelling the role of cell-cell adhesion in the growth and development of carcinoma, Mathematical and computer modelling 24(12) (1996) 1-17.
[48] X. Zheng, S. Wise, V. Cristini, Nonlinear simulation of tumor necrosis, neo-vascularization and tissue invasion via an adaptive finite-element/level-set method, Bulletin of mathematical biology 67(2) (2005) 211-259.
[49] K. Pham, H.B. Frieboes, V. Cristini, J. Lowengrub, Predictions of tumour morphological stability and evaluation against experimental observations, Journal of the Royal Society Interface 8(54) (2011) 16-29.
[50] M. Carmen Calzada, G. Camacho, E. Fernández-Cara, M. Marín, Fictitious domains and level sets for moving boundary problems. Applications to the numerical simulation of tumor growth, Journal of Computational Physics 230(4) (2011) 1335-1358.
[51] M. Wu, H.B. Frieboes, S.R. McDougall, M.A.J. Chaplain, V. Cristini, J. Lowengrub, The effect of interstitial pressure on tumor growth: Coupling with the blood and lymphatic vascular systems, Journal of theoretical biology 320 (2013) 131-151.
[52] J.J. Lee, J. Huang, C.G. England, L.R. McNally, H.B. Frieboes, Predictive Modeling of In Vivo Response to Gemcitabine in Pancreatic Cancer, PLoS computational biology 9(9) (2013) e1003231.
[53] J. Ovadia, Q. Nie, Numerical Methods for Two-Dimensional Stem Cell Tissue Growth, Journal of scientific computing 58(1) (2014) 149-175.
[54] H.P. Greenspan, On the growth and stability of cell cultures and solid tumors, Journal of theoretical biology 56(1) (1976) 229-42.
[55] P. Macklin, S. Mumenthaler, J. Lowengrub, Modeling multiscale necrotic and calcified tissue biomechanics in cancer patients: application to ductal carcinoma in situ (DCIS), Multiscale Computer Modeling in Biomechanics and Biomedical Engineering, Springer2013, pp. 349-380.
[56] H. Rubin, Microenvironmental regulation of the initiated cell, Advances in cancer research 90 (2003) 1-62.
[57] P. Ciarletta, L. Foret, M.B. Amar, The radial growth phase of malignant melanoma: multi-phase modelling, numerical simulations and linear stability analysis, J R Soc Interface 8(56) (2011) 345-368.
[58] M.B. Amar, C. Chatelain, P. Ciarletta, Contour instabilities in early tumor growth models, Physical review letters 106(14) (2011) 148101.

[59] P. Vaupel, F. Kallinowski, P. Okunieff, Blood flow, oxygen and nutrient supply, and metabolic microenvironment of human tumors: a review, Cancer research 49(23) (1989) 6449-65.
[60] K. Garber, Energy boost: the Warburg effect returns in a new theory of cancer, Journal of the National Cancer Institute 96(24) (2004) 1805-6.
[61] M.A. Esteban, P.H. Maxwell, HIF, a missing link between metabolism and cancer, Nature medicine 11(10) (2005) 1047-8.
[62] J.E. Testa, Loss of the metastatic phenotype by a human epidermoid carcinoma cell line, HEp-3, is accompanied by increased expression of tissue inhibitor of metalloproteinase 2, Cancer research 52(20) (1992) 5597-603.
[63] P. Macklin, S. McDougall, A.R. Anderson, M.A. Chaplain, V. Cristini, J. Lowengrub, Multiscale modelling and nonlinear simulation of vascular tumour growth, Journal of mathematical biology 58(4-5) (2009) 765-98.
[64] A.R. Anderson, A hybrid mathematical model of solid tumour invasion: the importance of cell adhesion, Mathematical medicine and biology : a journal of the IMA 22(2) (2005) 163-86.
[65] M.H. Zaman, L.M. Trapani, A.L. Sieminski, D. Mackellar, H. Gong, R.D. Kamm, A. Wells, D.A. Lauffenburger, P. Matsudaira, Migration of tumor cells in 3D matrices is governed by matrix stiffness along with cell-matrix adhesion and proteolysis, Proceedings of the National Academy of Sciences of the United States of America 103(29) (2006) 10889-94.
[66] D. Gonzalez-Rodriguez, K. Guevorkian, S. Douezan, F. Brochard-Wyart, Soft matter models of developing tissues and tumors, Science (New York, N.Y.) 338(6109) (2012) 910-7.
[67] R.A. Foty, C.M. Pfleger, G. Forgacs, M.S. Steinberg, Surface tensions of embryonic tissues predict their mutual envelopment behavior, Development 122(5) (1996) 1611-1620.
[68] A.R. Anderson, M. Chaplain, Continuous and discrete mathematical models of tumor-induced angiogenesis, Bulletin of mathematical biology 60(5) (1998) 857-899.
[69] V.P. Terranova, R. DiFlorio, R.M. Lyall, S. Hic, R. Friesel, T. Maciag, Human endothelial cells are chemotactic to endothelial cell growth factor and heparin, J Cell Biol 101(6) (1985) 2330-2334.
[70] A.R.A. Anderson, M.A.J. Chaplain, E.L. Newman, R.J.C. Steele, A.M. Thompson, Mathematical Modelling of Tumour Invasion and Metastasis, Journal of Theoretical Medicine 2(2) (2000) 129-154.
[71] R.C. Aldredge, Semi-Lagrangian advection–propagation (SLAP) scheme for three-dimensional interface tracking, Journal of Computational Physics 229(12) (2010) 4683-4702.
[72] B.P. Leonard, Universal limiter for transient interpolation modeling of the advective transport equations: the ULTIMATE conservative difference scheme, NASA Technical Memorandum 100916 (1988).
[73] B.P. Leonard, MacVean MK, Lock AP, Positivity-preserving numerical schemes for multidimensional advection, NASA Technical Memorandum 106055 (1993).
[74] Z. Li, K. Ito, The immersed interface method: numerical solutions of PDEs involving interfaces and irregular domains, Siam2006.
[75] D.P. Peng, B. Merriman, S. Osher, H.K. Zhao, M.J. Kang, A PDE-based fast local level set method, Journal of Computational Physics 155(2) (1999) 410-438.
[76] J.A. Sethian, P. Smereka, Level set methods for fluid interfaces, Annual Review of Fluid Mechanics 35 (2003) 341-372.
[77] G.-S. Jiang, D. Peng, Weighted ENO schemes for Hamilton--Jacobi equations, SIAM Journal on Scientific computing 21(6) (2000) 2126-2143.
[78] P. Macklin, J. Lowengrub, An improved geometry-aware curvature discretization for level set methods: Application to tumor growth, Journal of Computational Physics 215(2) (2006) 392-401.
[79] D.W. Peaceman, H.H. Rachford, The Numerical Solution of Parabolic and Elliptic Differential Equations, Journal of the Society for Industrial and Applied Mathematics 3(1) (1955) 28-41.
[80] M. Kolev, B. Zubik-Kowal, Numerical solutions for a model of tissue invasion and migration of tumour cells, Computational and mathematical methods in medicine 2011 (2011) 452320.

[81] U. Cavallaro, G. Christofori, Cell adhesion and signalling by cadherins and Ig-CAMs in cancer, Nature Reviews Cancer 4(2) (2004) 118-132.
[82] M. Takeichi, Cadherins in cancer: implications for invasion and metastasis, Current opinion in cell biology 5(5) (1993) 806-811.
[83] U.H. Frixen, J. Behrens, M. Sachs, G. Eberle, B. Voss, A. Warda, D. Lochner, W. Birchmeier, E-cadherin-mediated cell-cell adhesion prevents invasiveness of human carcinoma cells, The Journal of cell biology 113(1) (1991) 173-85.
[84] A.L. Harris, Hypoxia—a key regulatory factor in tumour growth, Nature Reviews Cancer 2(1) (2002) 38-47.
[85] D. Hanahan, R.A. Weinberg, Hallmarks of cancer: the next generation, Cell 144(5) (2011) 646-674.
[86] L.M. Coussens, B. Fingleton, L.M. Matrisian, Matrix metalloproteinase inhibitors and cancer: trials and tribulations, Science (New York, N.Y.) 295(5564) (2002) 2387-92.

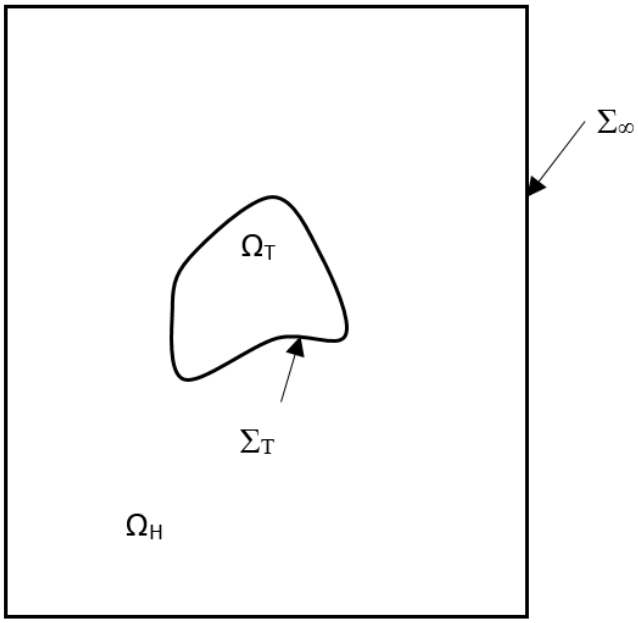

Figure 1: Computational domain displaying the tumor enclosed in host tissue

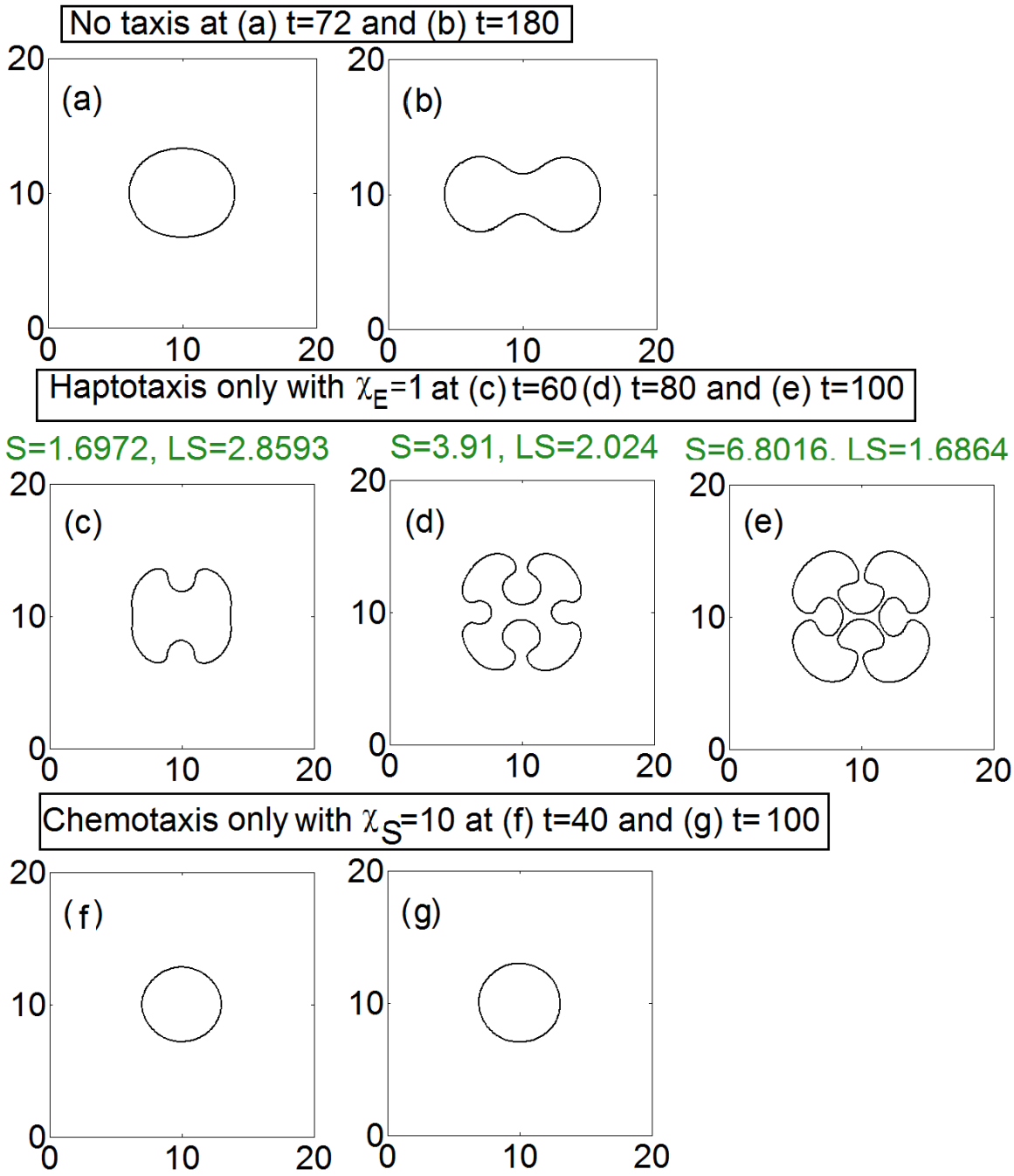

Figure 2: Tumor boundary in nutrient-poor environment for no taxis, haptotaxis only and chemotaxis only

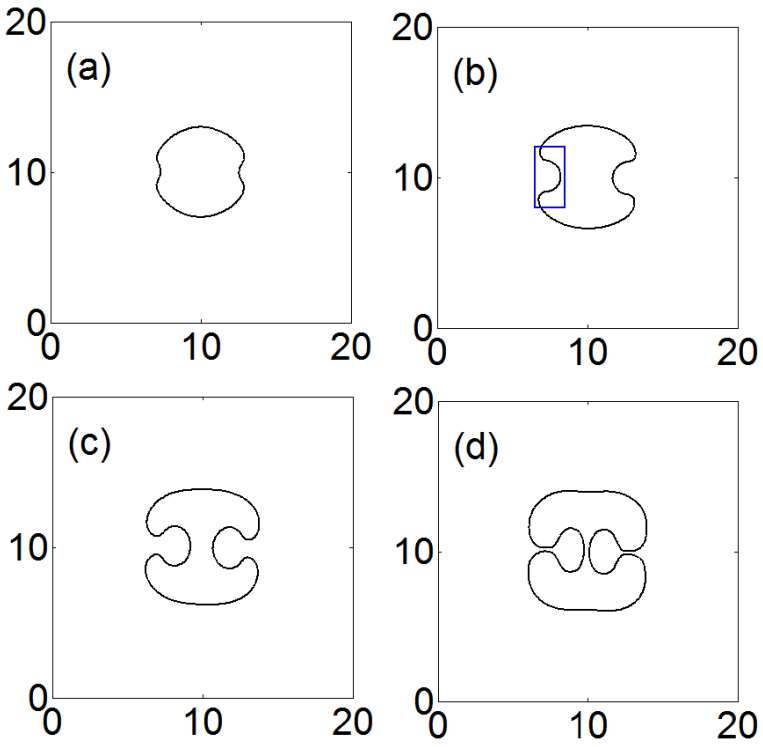

Figure 3: Tumor boundary for χ_E =1 and χ_S =10 in nutrient-poor environment at (a) t=40, (b) t=60, (c) t=80 and (d) t=100

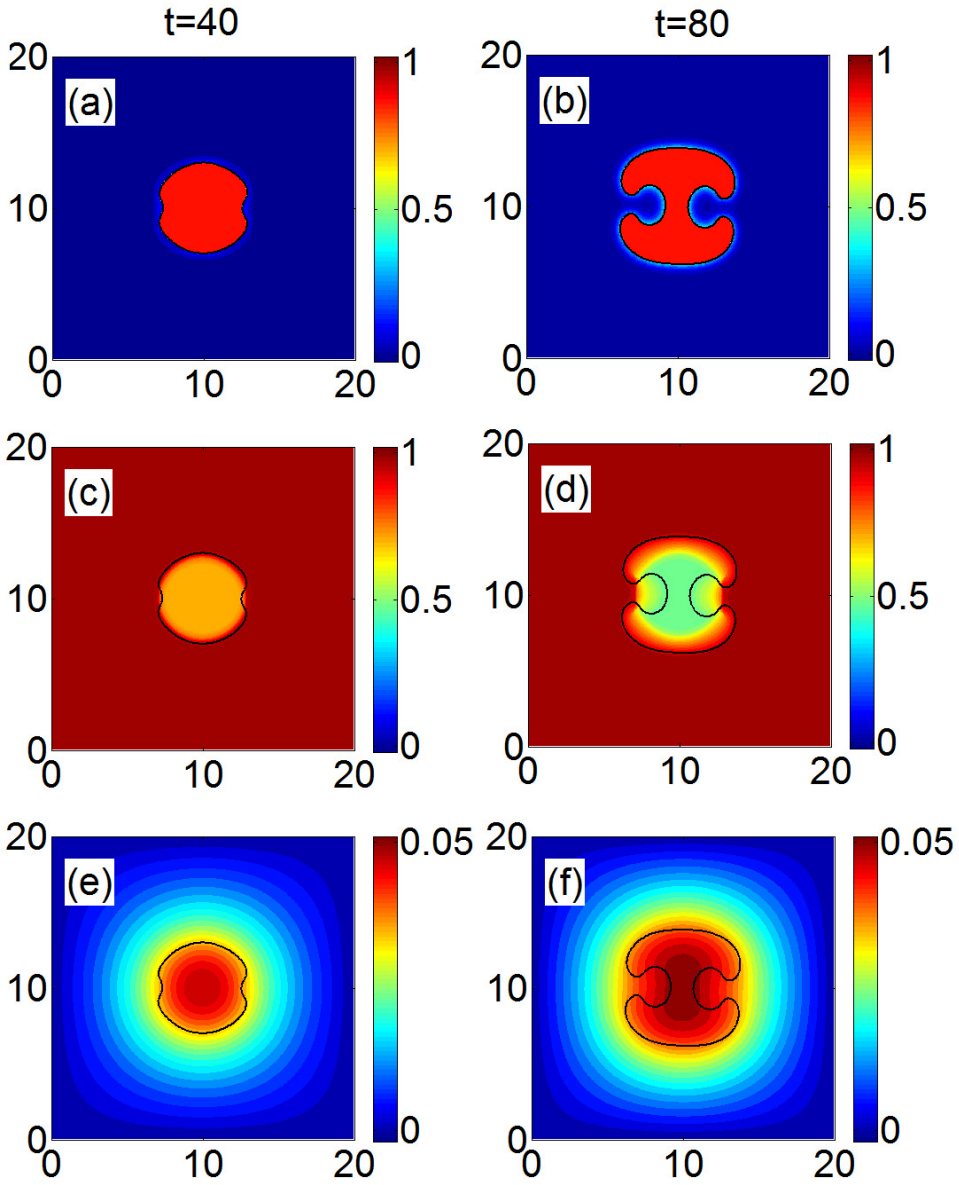

Figure 4: Contours of MDE ((a) and (b)), ECM ((c) and (d)) and soluble ECM ((e) and (f)) at t=40 and 80 respectively

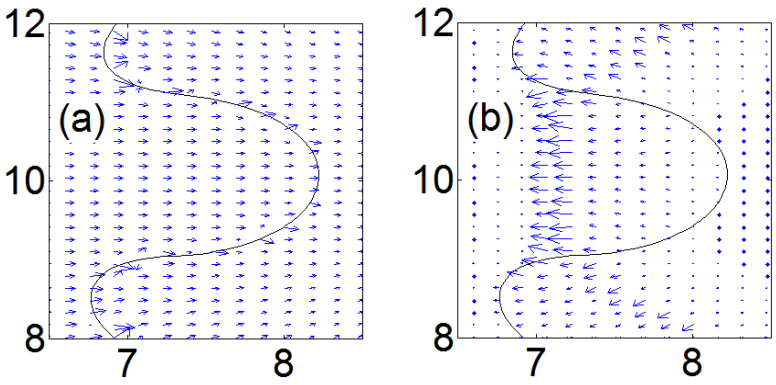

Figure 5: Gradients (near left bulge inside blue box in Fig. 3b) in nutrient-poor environment for χ_E =1 and χ_S =10 at t=60 (a) Soluble ECM (the longest arrow corresponds to a length of 0.026543) and (b) ECM (the longest arrow corresponds to 1.21351)

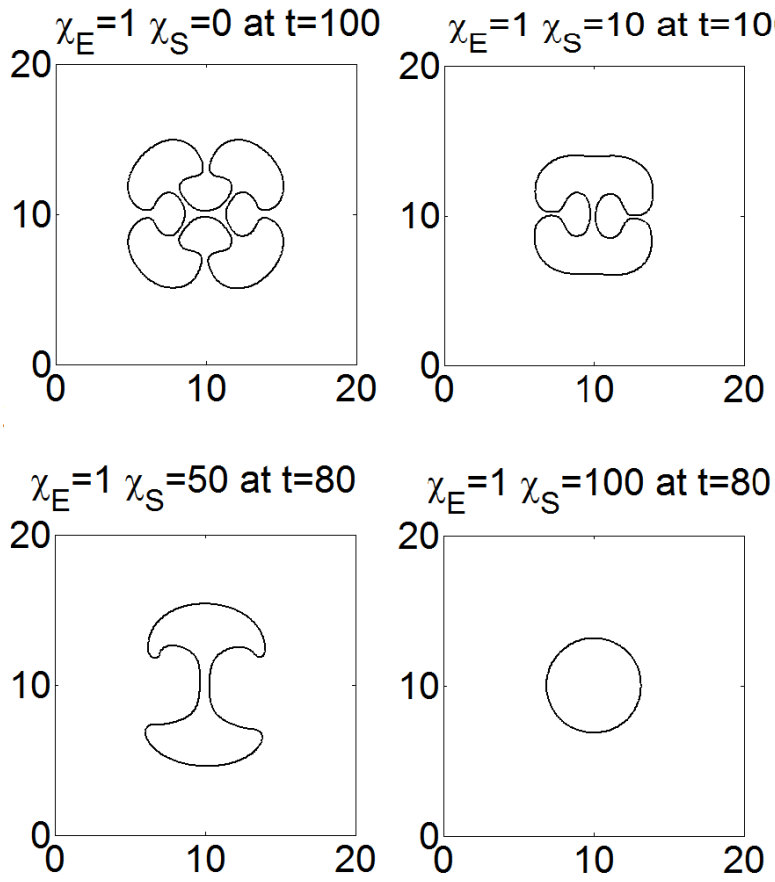

Figure 6: Effect of chemotaxis on tumor morphology for nutrient-poor microenvironment

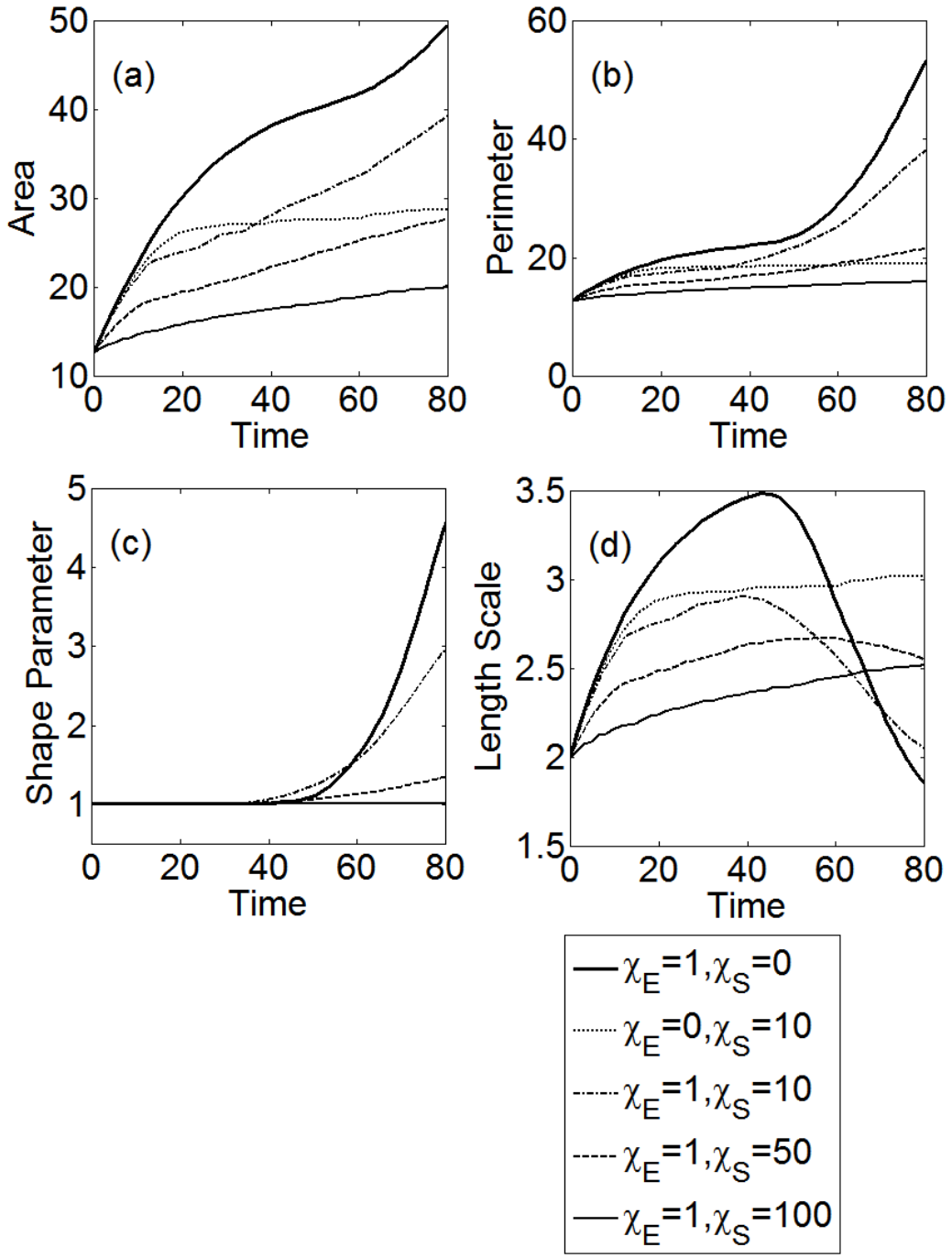

Figure 7: Effect of different chemotaxis coefficients on tumor growth and morphology for nutrient-poor microenvironment

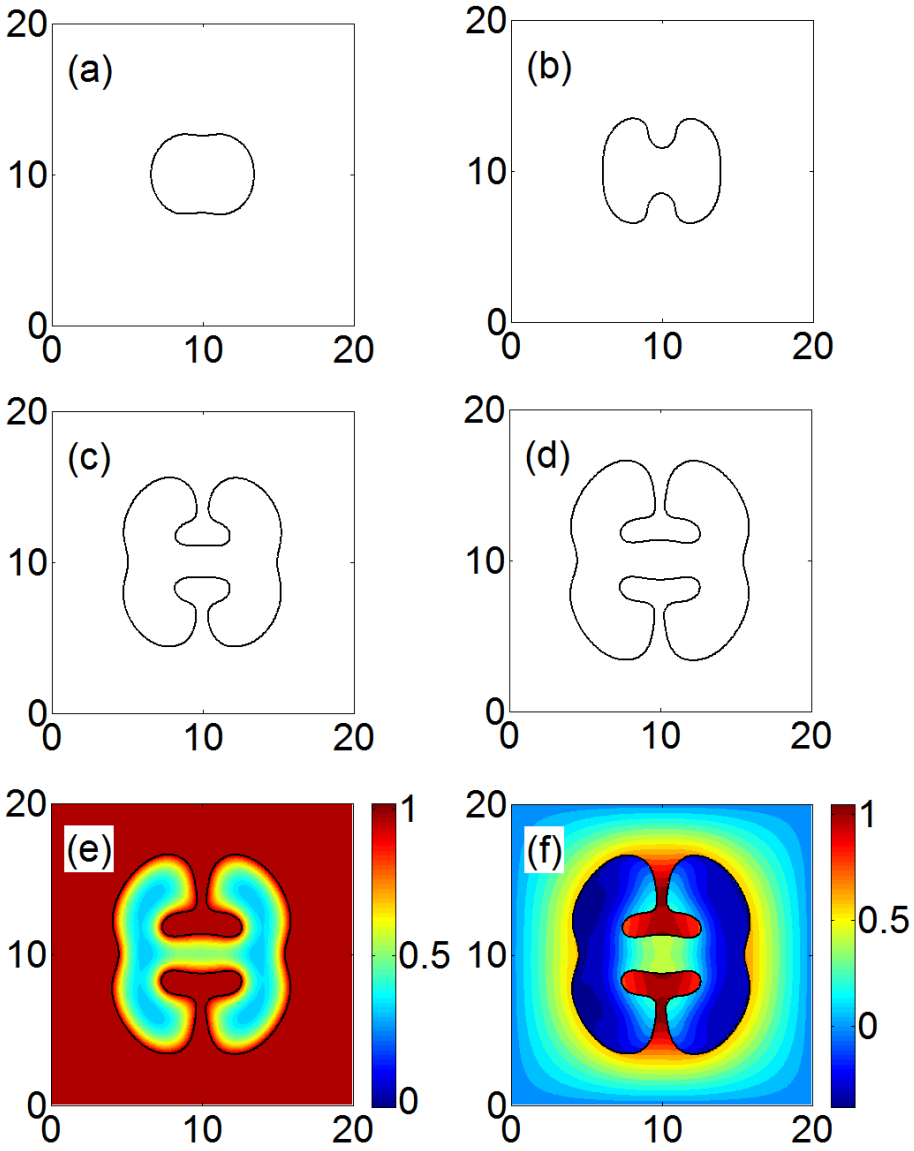

Figure 8: Tumor boundary for χ_E =1 in nutrient-rich environment at (a) 24 (b) t=36, (c) t=48 (d) t=52 and (e) nutrient and (f) net pressure contours at t=52

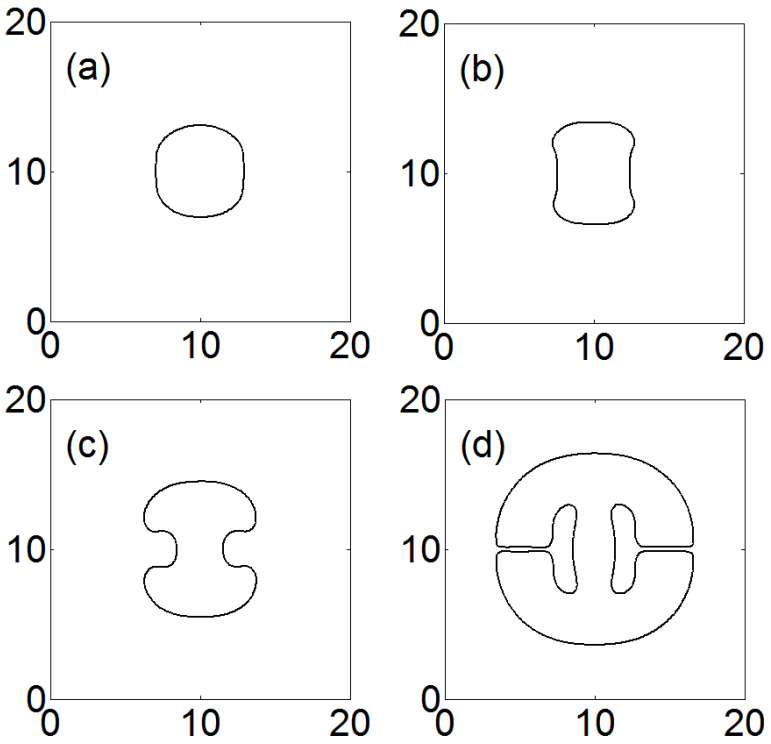

Figure 9: Tumor boundary for χ_E =1 and χ_S =50 in nutrient-rich environment at (a) t=40, (b) t=60, (c) t=80 and (d) t= 100

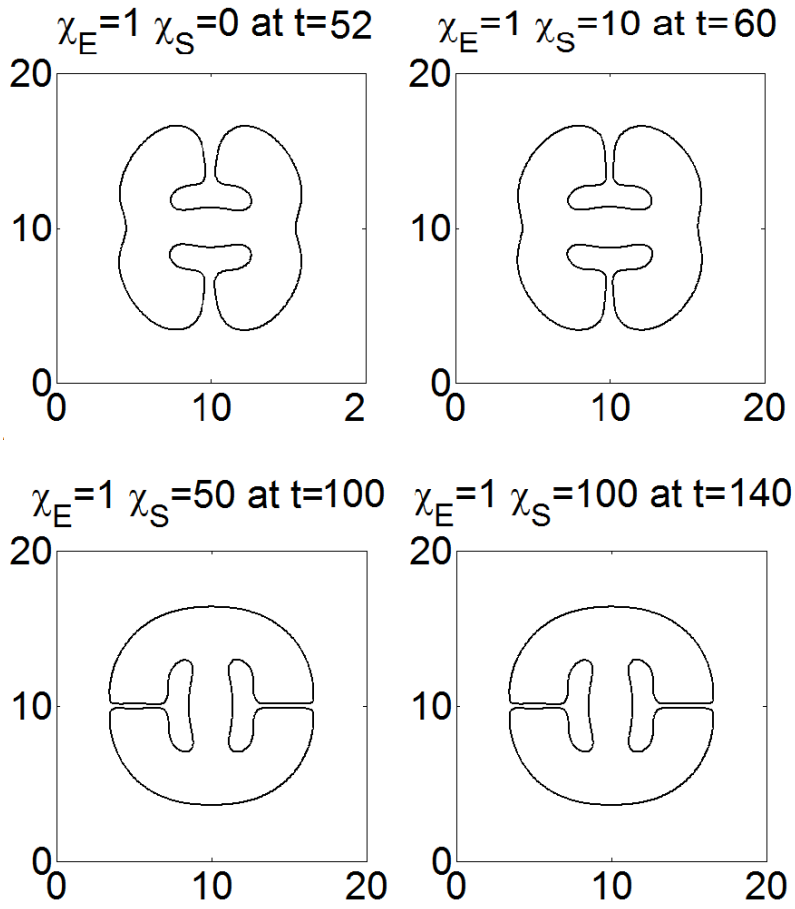

Figure 10: Effect of different extents of chemotaxis on tumor morphology for nutrient-rich microenvironment

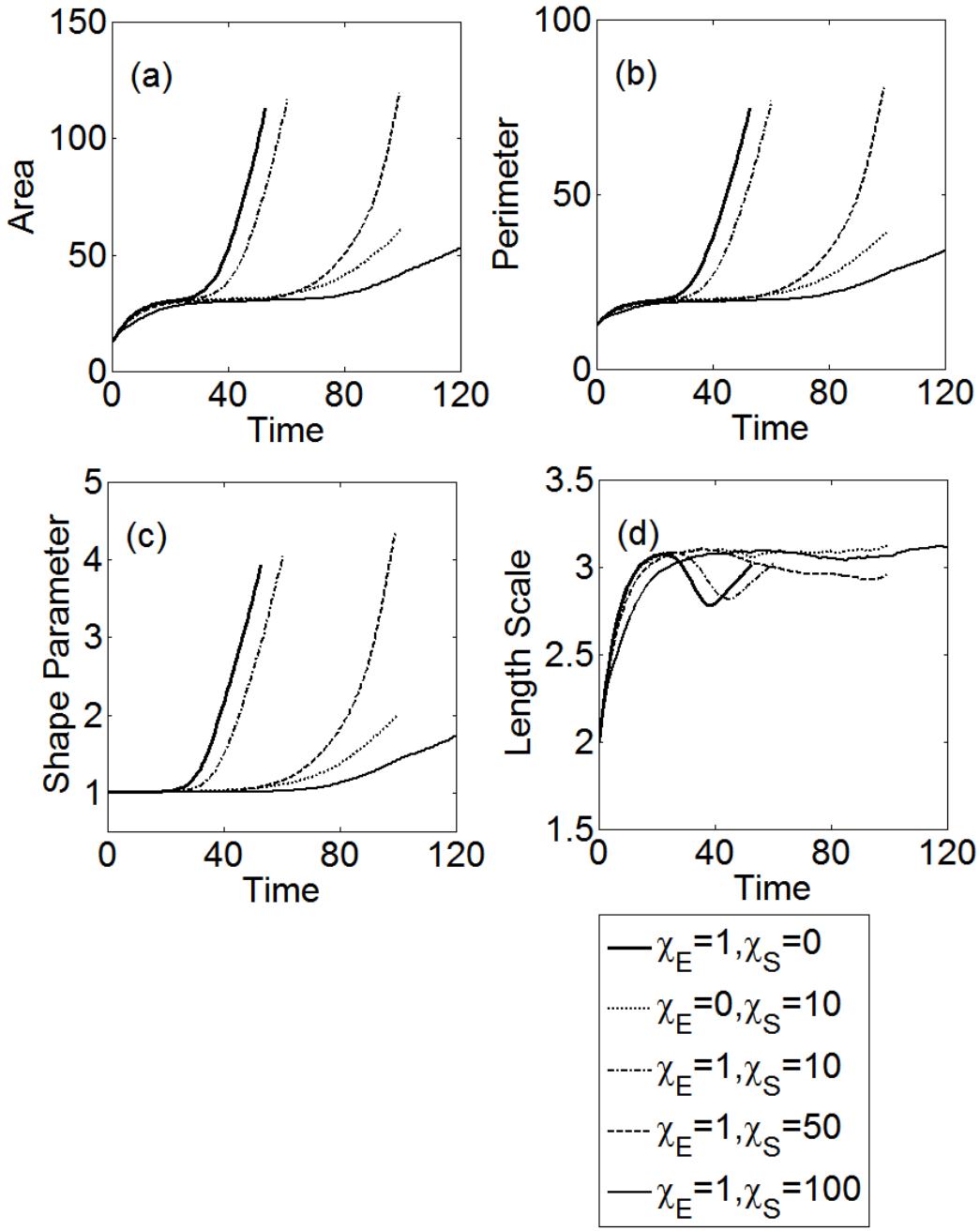

Figure 11: Effect of chemotaxis coefficient on tumor growth and morphology for nutrient-rich microenvironment (thick solid line for χ_E =1 and χ_S =0, dotted line for χ_E =0 and χ_S =10, dash-dotted line for χ_E =1 and χ_S =10, dashed line for χ_E =1 and χ_S =50, thin solid line χ_E =1 and χ_S =100)

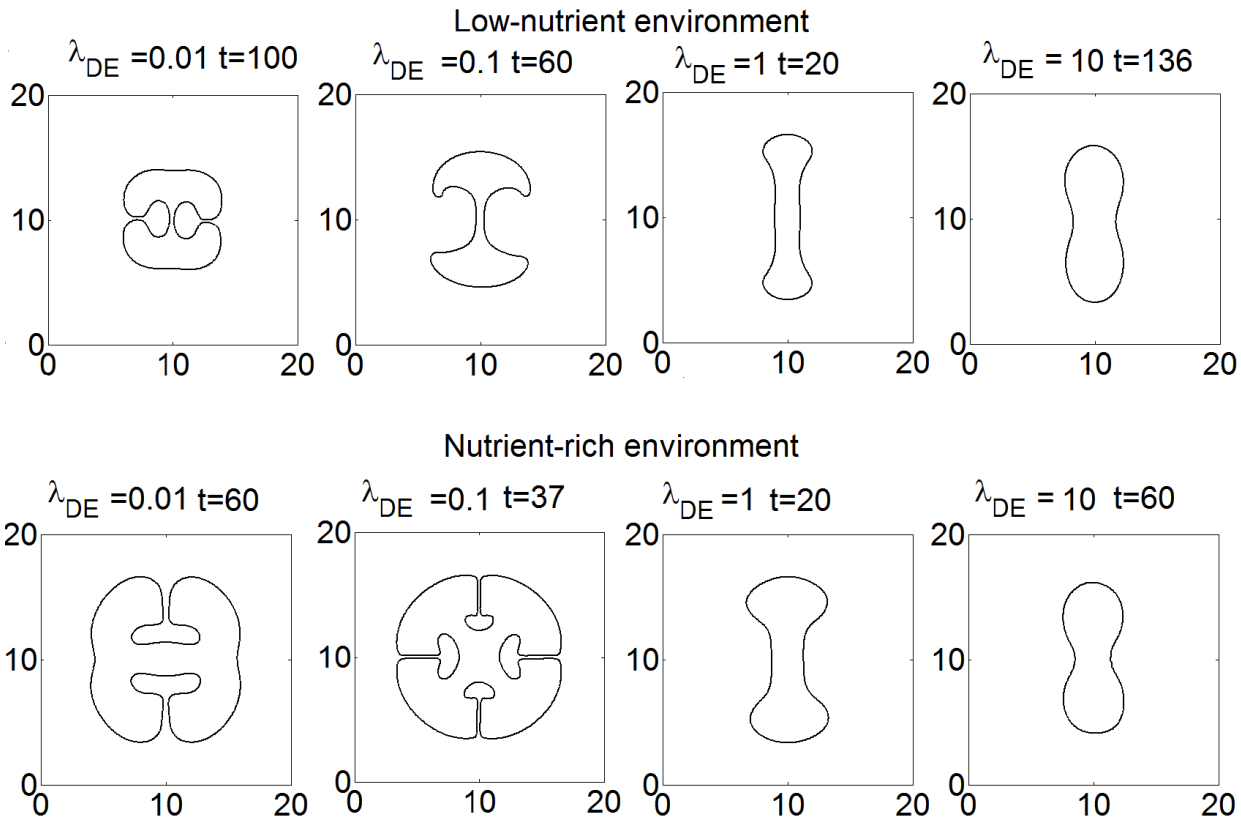

Figure 12: Effect of ECM degradation rate, λ_{DE} on tumor morphology with χ_E =1, χ_S =10, λ_M=100 and k_S=1

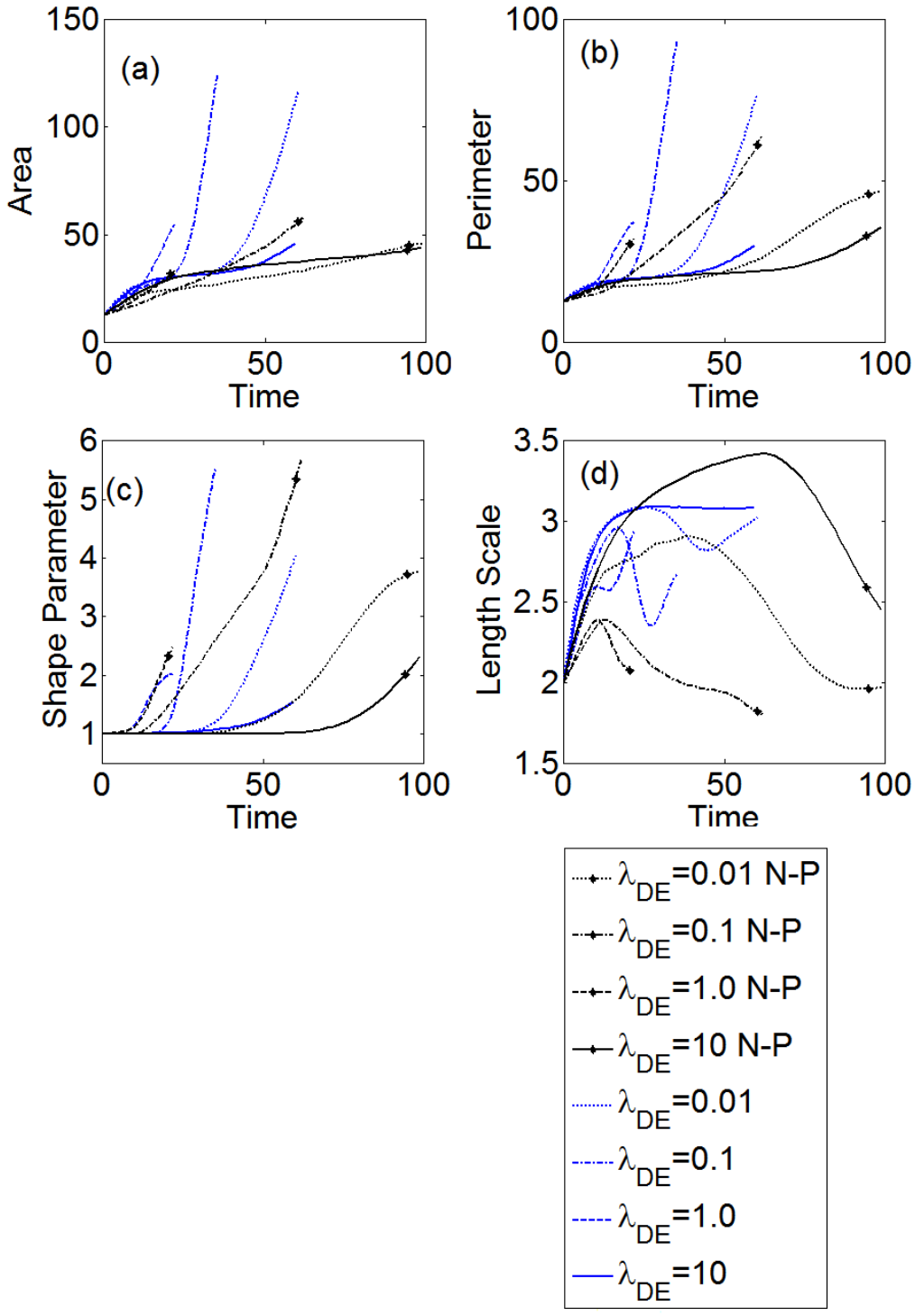

Figure 13: Effect of ECM degradation rate, λ_{DE} on tumor growth and morphology for χ_E =1, χ_S =10 and nutrient-rich (blue line) and nutrient-poor (N-P) (black line with * marker point) microenvironment.

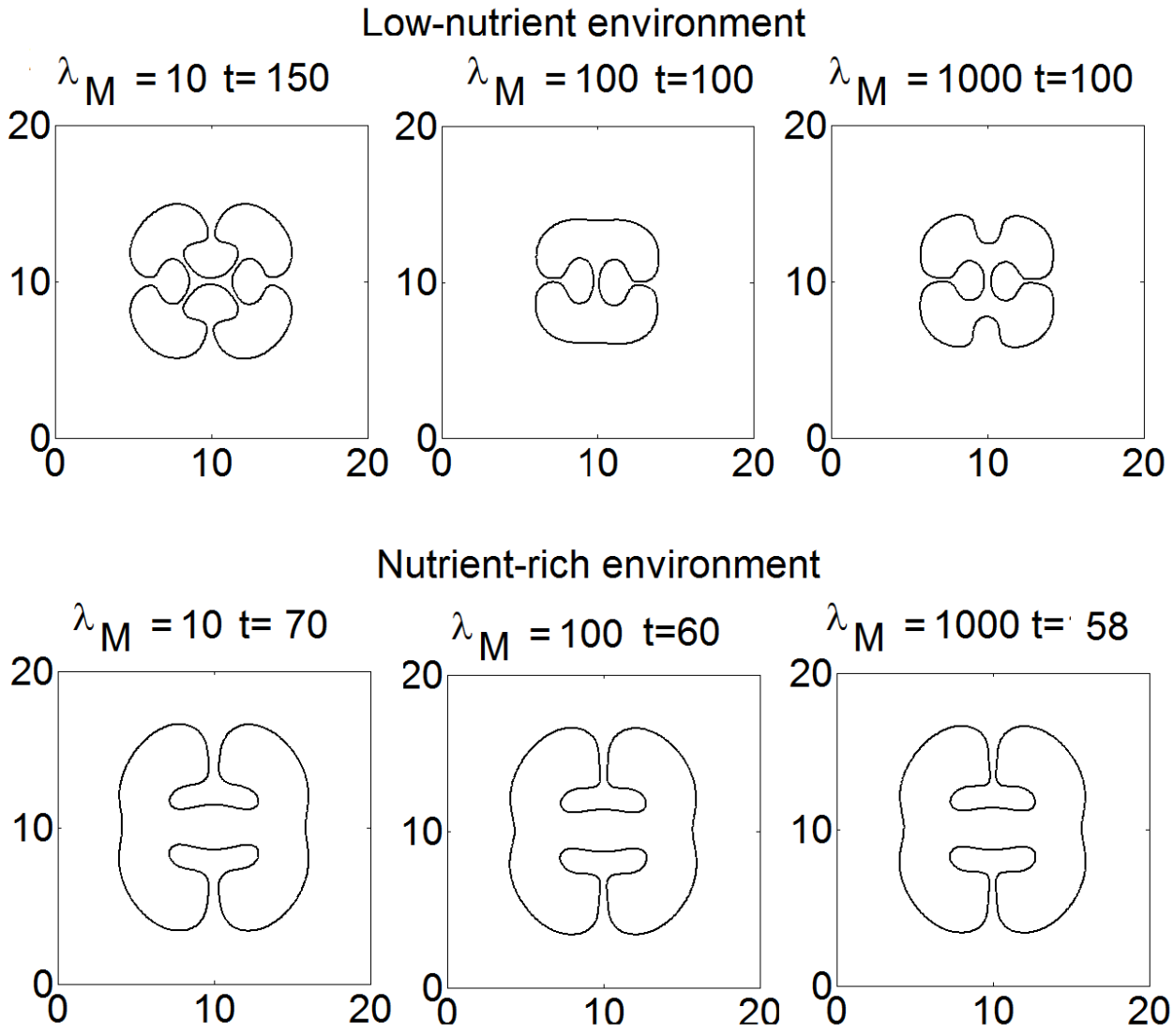

Figure 14: Effect of MDE production rate, λ_M on tumor morphology with χ_E =1, χ_S =10, λ_{DE}=0.01 and k_S=1

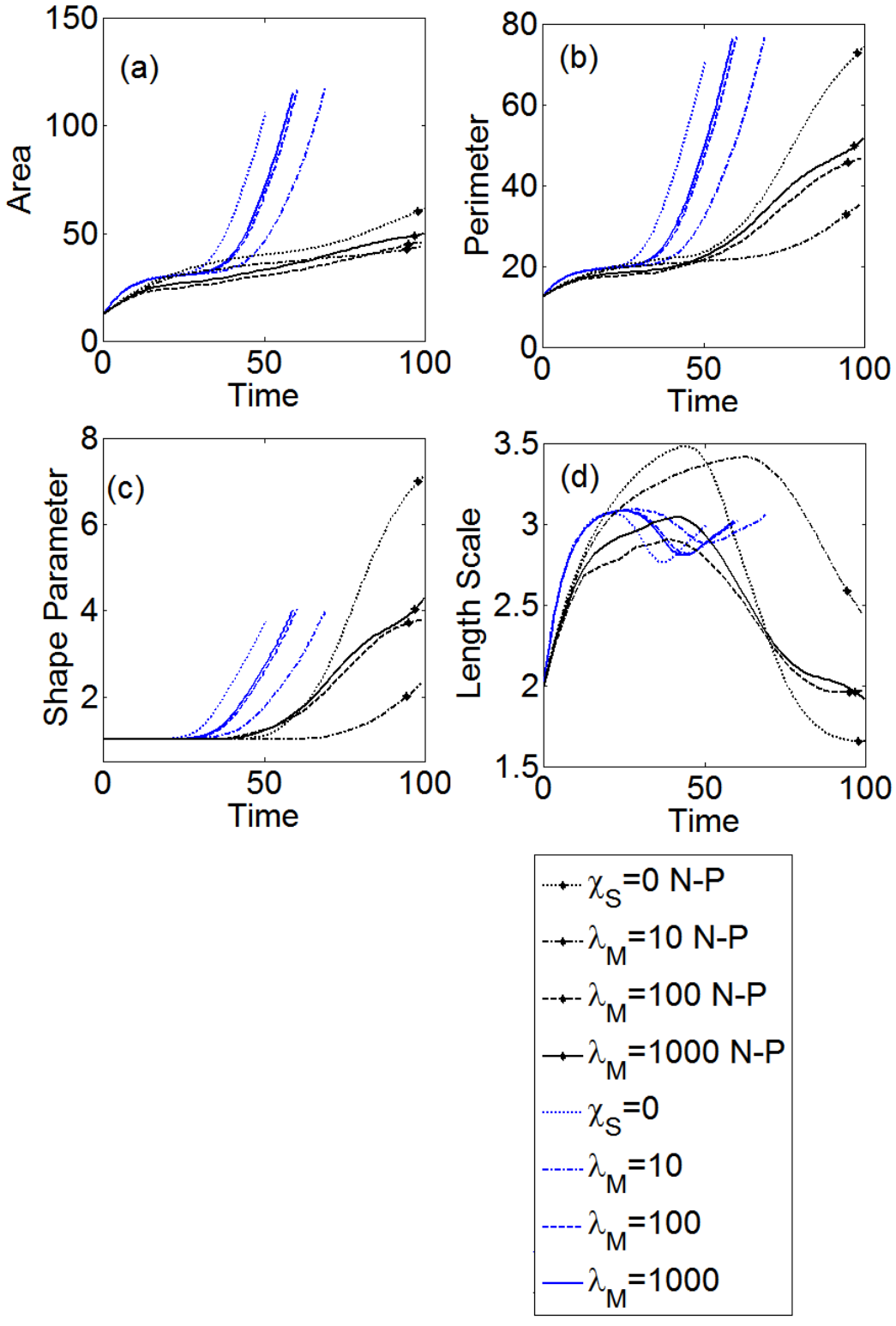

Figure 15: Effect of MDE production rate, λ_M on tumor growth and morphology for χ_E =1 and χ_S =10 for nutrient-rich (blue line) and nutrient-poor (N-P) (black line with * marker point) microenvironment.

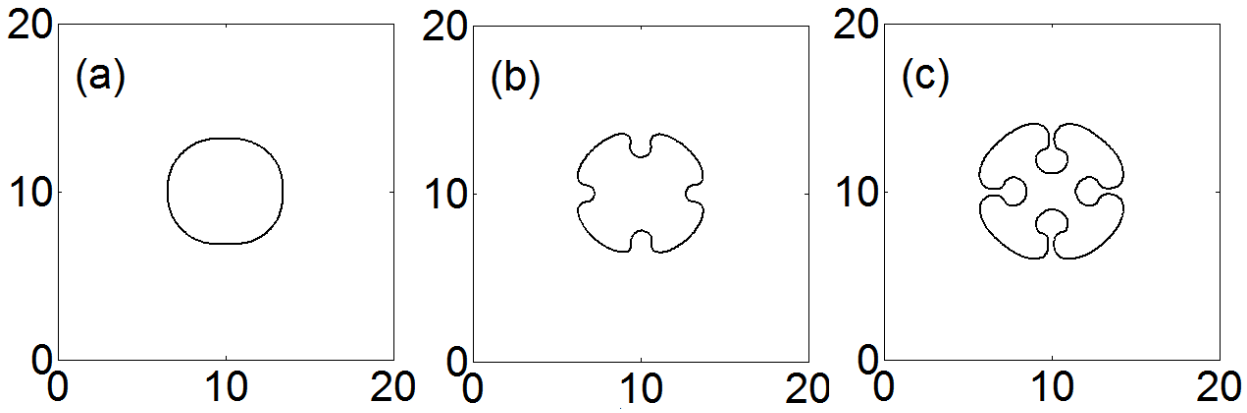

Figure 16: Tumor boundary for low surface tension $\Gamma = 0.01$, $\chi_E = 1$ and $\chi_S = 10$ at (a) t=40 (b) t=60 and (c) t=80

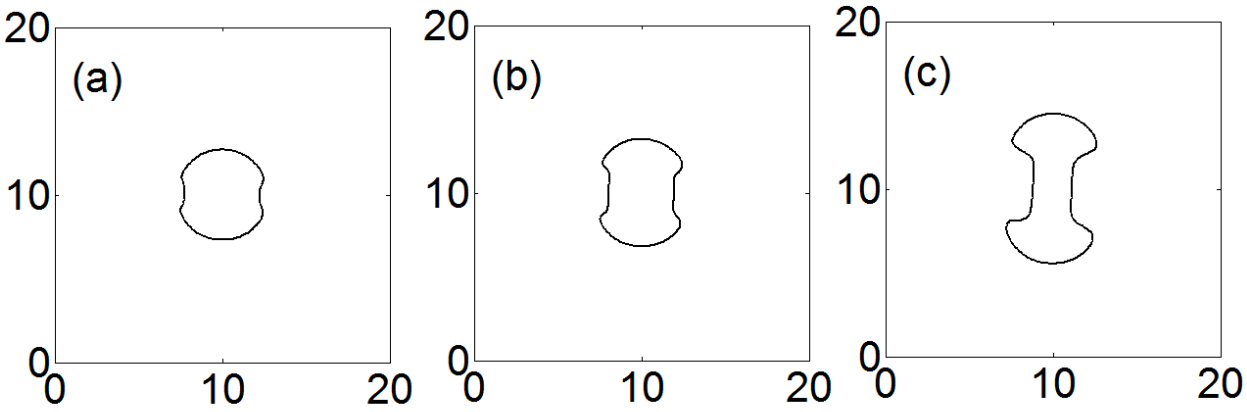

Figure 17: Tumor boundary for $\Gamma = 0.01$, $\chi_E = 1$ and $\chi_S = 50$ at (a) t=40 (b) t=60 and (c) t=80

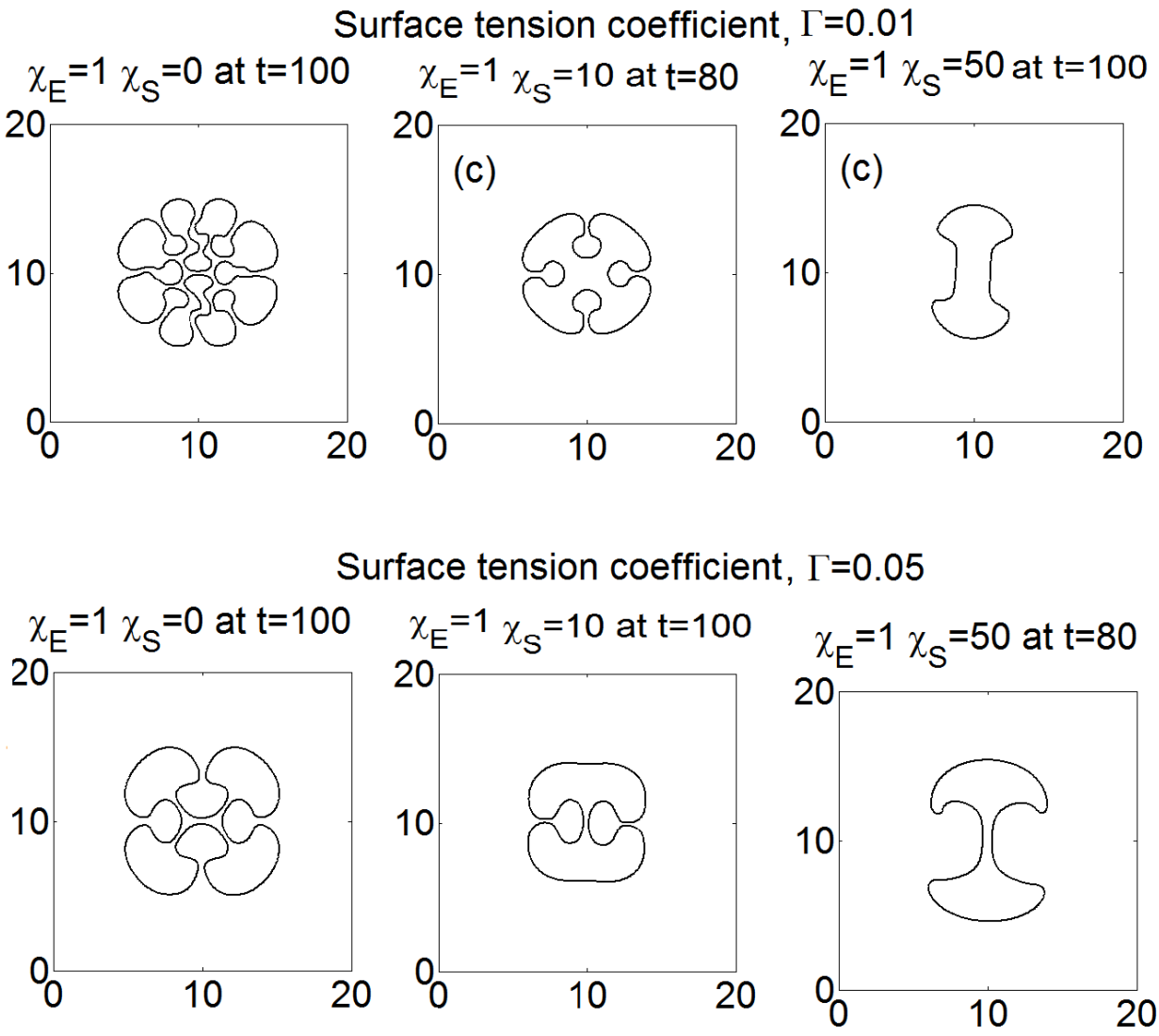

Figure 18: Effect of chemotaxis on tumor morphology for different surface tensions

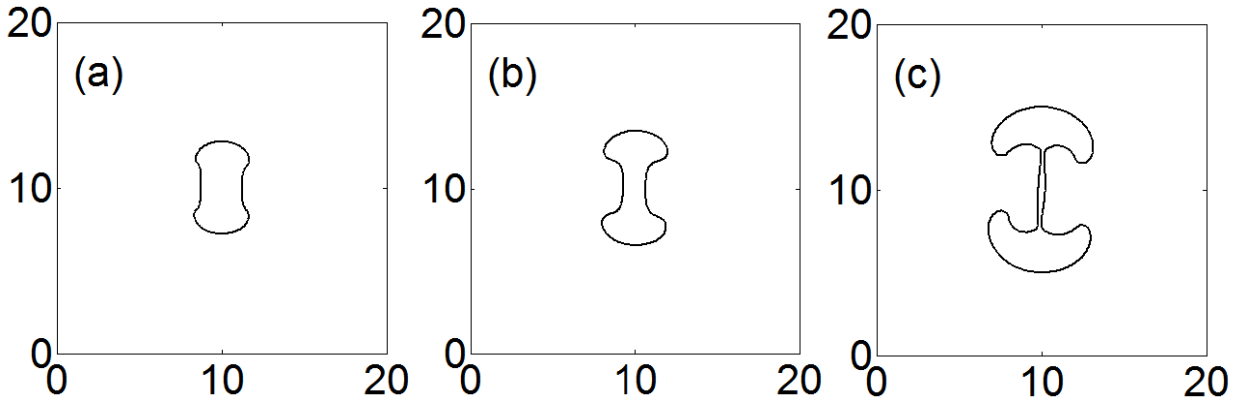

Figure 19: Tumor boundary for low proliferation case with χ_E =1 and χ_S =10 at (a) t=30 (b) t=45 (c) t=60, (d) t=75

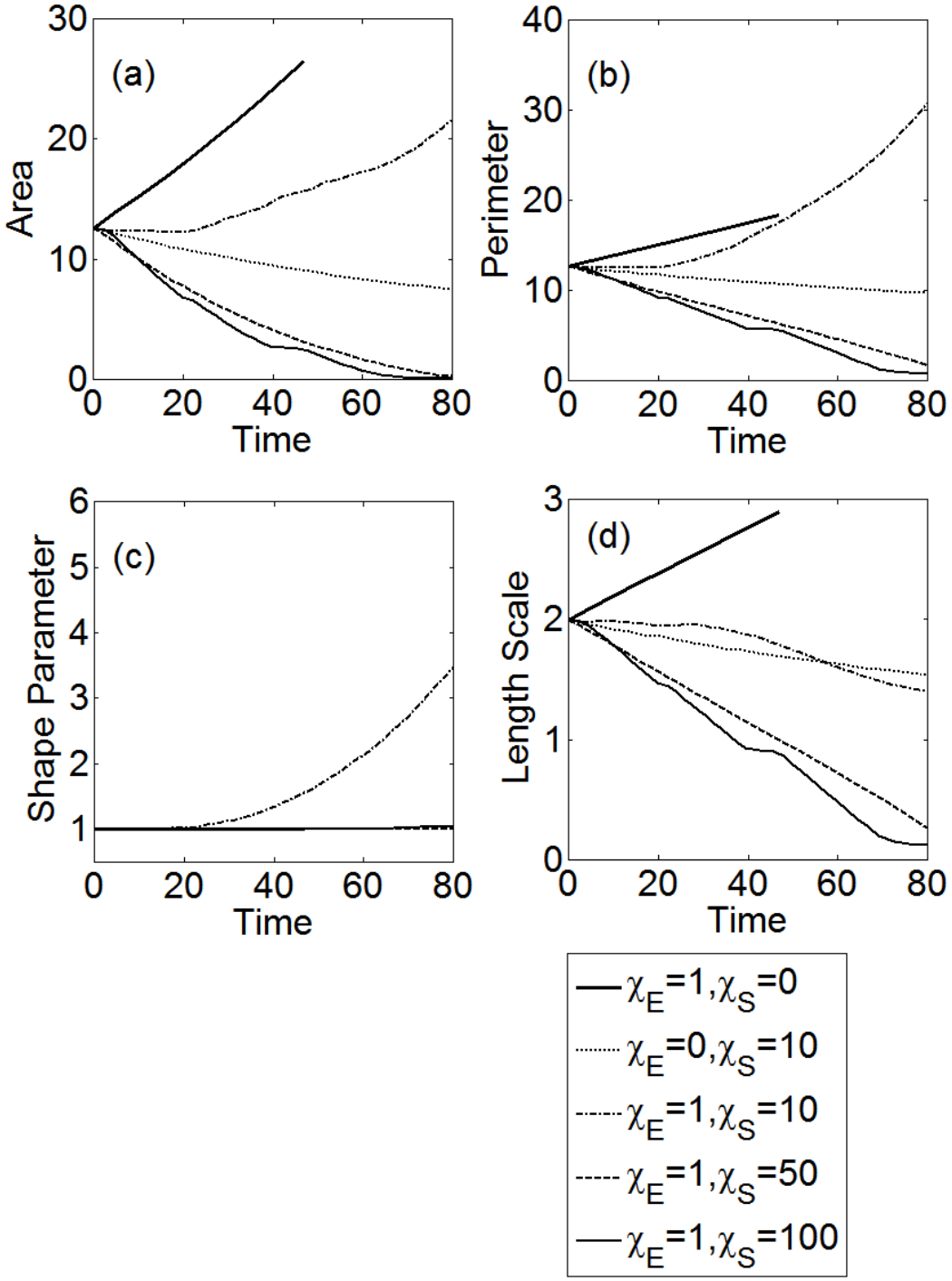

Figure 20: Effect of chemotaxis coefficient on tumor growth and morphology for hypoxic low-proliferation environment (thick solid line for χ_E =1 and χ_S =0, dotted line for χ_E =0 and χ_S =10, dash-dotted line for χ_E =1 and χ_S =10, dashed line for χ_E =1 and χ_S =50, thin solid line χ_E =1 and χ_S =100)

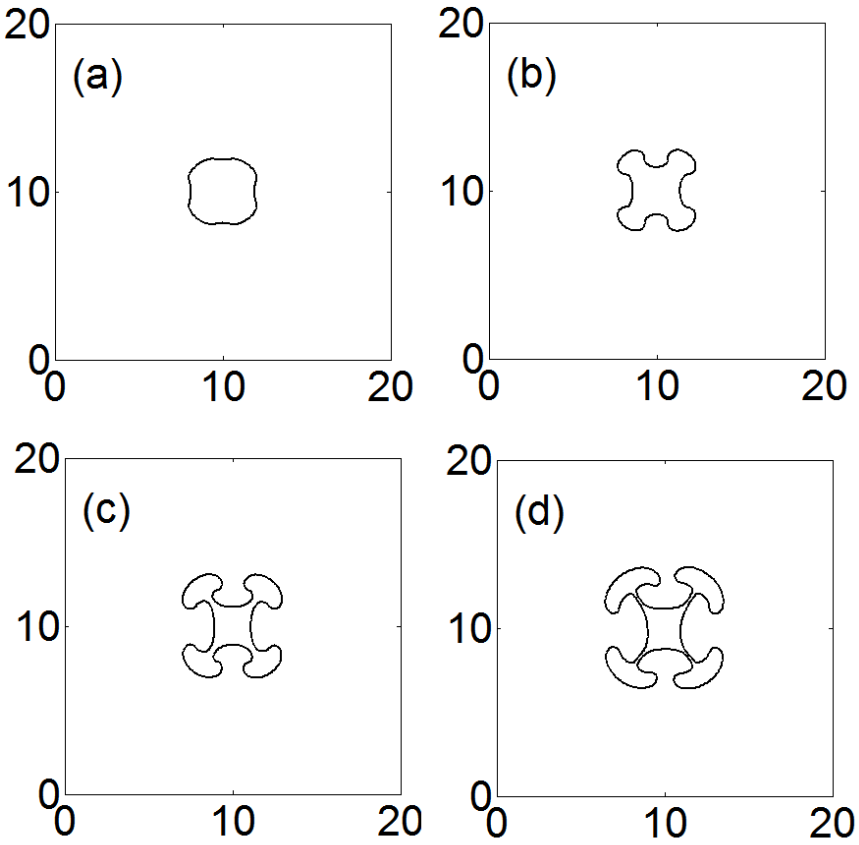

Figure 21: Tumor boundary for λ_P=0.1, χ_E =5 and χ_S =10 at (a) t=10, (b) t=20, (c) t=30 and (d) t=40

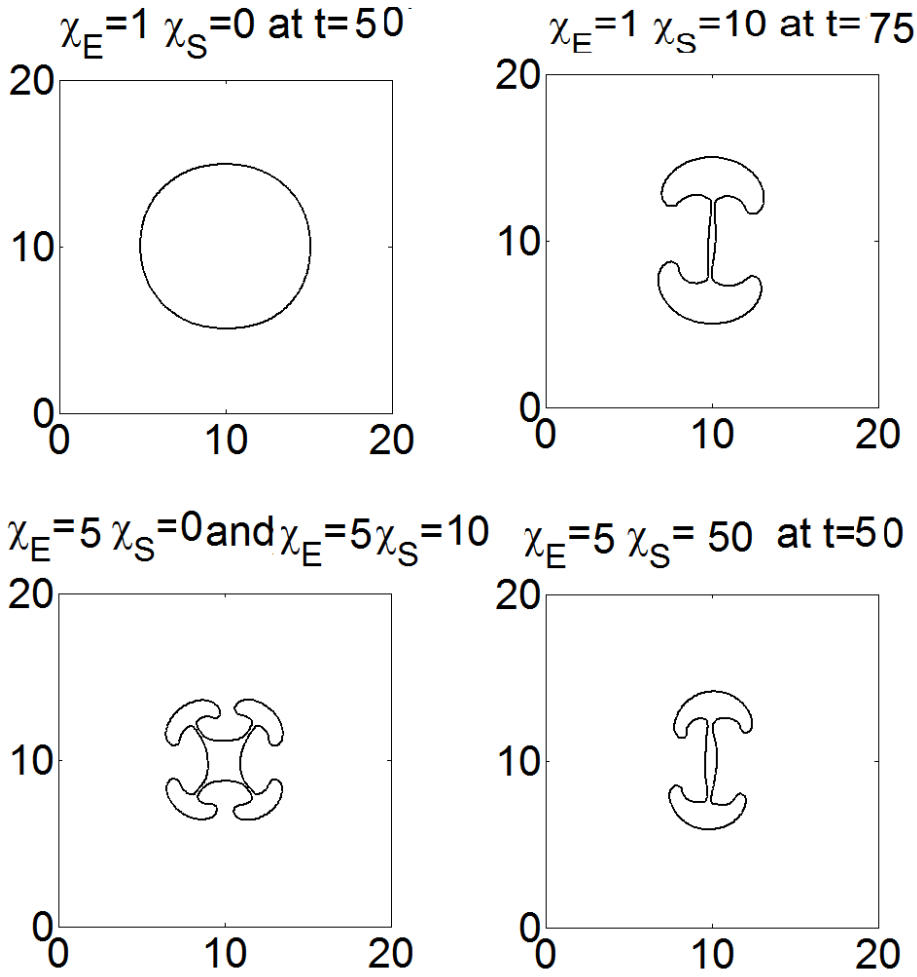

Figure 22: Effect of chemotaxis on tumor shape for hypoxic low-proliferation microenvironment

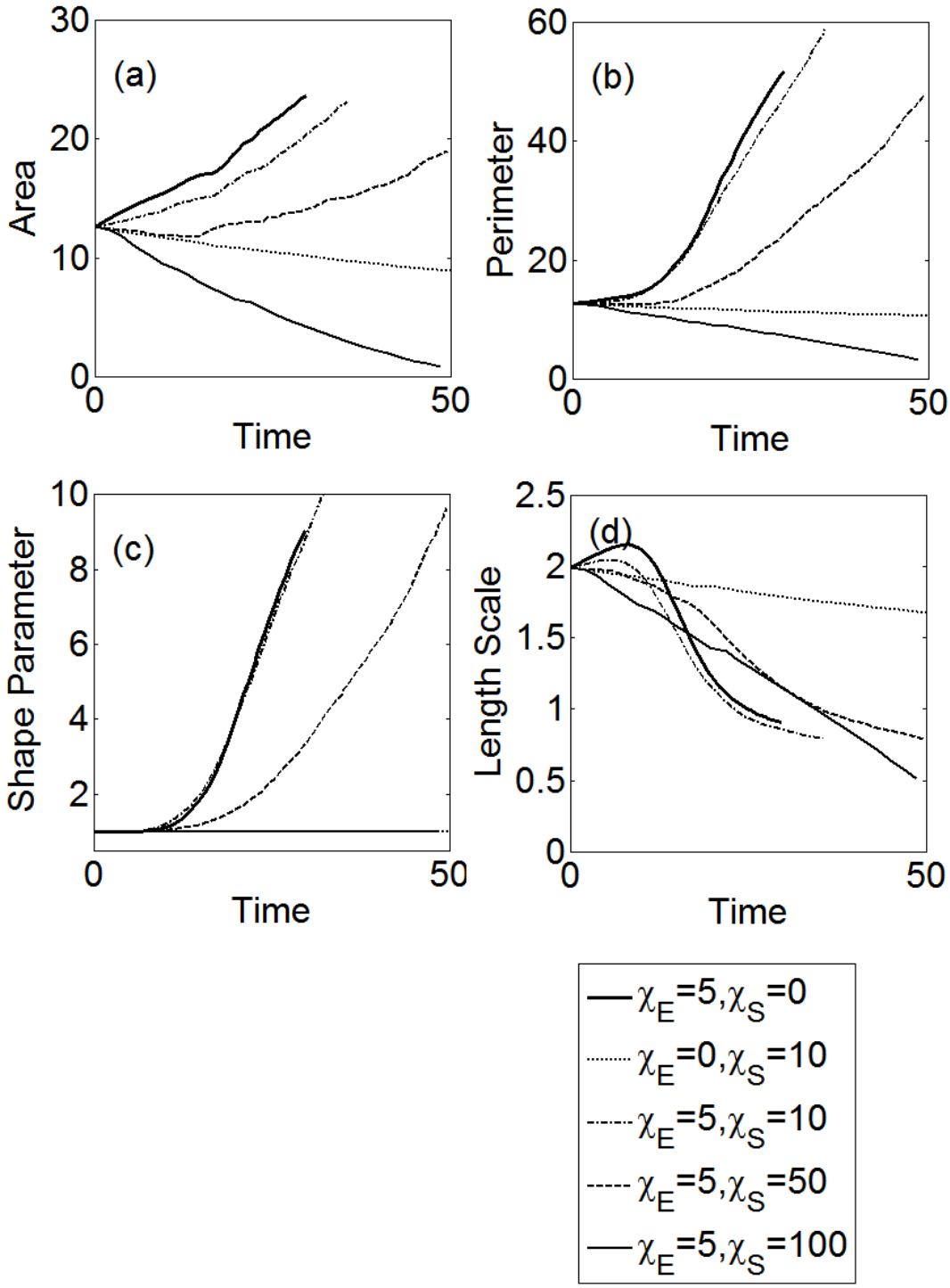

Figure 23: Effect of chemotaxis coefficient on tumor growth and morphology for hypoxic low-proliferation microenvironment (thick solid line for χ_E =5 and χ_S =0, dotted line for χ_E =0 and χ_S =10, dash-dotted line for χ_E =5 and χ_S =10, dashed line for χ_E =5 and χ_S =50, thin solid line χ_E =5 and χ_S =100)

Table 1: List of Dimensionless Variables

Dimensionless variable	Symbol	Unit
Nutrient concentration	N	N
Intact ECM density	E	E
MDE density	M	$M0$
Soluble ECM density	S	E
Cell velocity	$\vec{u}$	$L/$ $p,\max$
Pressure	p	p_T

Table 2: List of Baseline Dimensionless Parameters

Parameter	Expression	Significance	Value	Dimensional value
MDE diffusion coefficient D_M	$D_M/(L^2\lambda_{P,max})$	MDE diffusion coefficient relative to characteristic diffusivity L^2/τ [1]	1	$3.086X10^{-9}$ cm^2/s
MDE decay rate λ_{DM}	$\lambda_{DM}/\lambda_{P,max}$	MDE decay rate relative to maximum tumor-cell proliferation rate [1]	10	15/day
MDE tumor-cell Production rate λ_M	$\lambda_M\rho_T/(\lambda_{P,max}\rho_{M0})$	MDE production rate relative to maximum tumor-cell proliferation rate [1]	100	150/day
ECM degradation rate λ_{DE}	$\lambda_{DE}/\lambda_{P,max}$	ECM degradation rate (by MDE) relative to maximum tumor-cell proliferation rate [1]	0.01	0.015/day
Surface tension coefficient Γ	$/Lp_T$	A measure of cell-cell and cell-ECM adhesion forces [2]	0.05	
Rate of mitosis λ_P	$\lambda_P/\lambda_{P,max}$	Mitosis rate relative to maximum tumor-cell proliferation rate[1]	1	1/1.5days
Rate of apoptosis, λ_A	$\lambda_A/\lambda_{P,max}$	Apoptosis rate relative to tumor-cell proliferation rate [3]	0.1 (Low-nutrient) 0.5 (High-nutrient)	0.1/1.5days (Low-nutrient) 0.5/1.5days (High-nutrient)
Diffusion coefficient of soluble ECM	$D_S/(L^2\lambda_{P,max})$	How fast soluble ECM diffuses in the length and time scale [4]	1	$3.086X10^{-9}$ cm^2/s
Chemotaxis coefficient, χ_S	$\frac{\chi_S\rho_{S_0}}{\lambda_{p,\max}L^2}$	The extent of chemotaxis of soluble ECM, gradients	10	
Haptotaxis coefficient, χ_E	$\frac{E\ E}{p,\max L^2}$	The extent of haptotaxis of intact ECM gradients [1]	1	2600 $cm^2/s/M$

Table 3: List of values

Parameter	Low-nutrient (Section 4.1)	High-nutrient (Section 4.2)
Apoptosis rate	0.1	0.5
Chemotaxis coefficient	10, 50 ,100	10, 50, 100, 500

Table 4: Effect of ECM degradation rate (λ_{DE}) on the time when the tumor shape parameter (S) is 1.5

Taxis Coefficients	λ_{DE}	Low-nutrient	Nutrient-rich
χ_E =1, χ_S =0	0.01	33	58.5
χ_E =1, χ_S =10	0.01	40	58.2
χ_E =1, χ_S =10	0.1	22.5	20.9
χ_E =1, χ_S =10	1	13.7	14.3
χ_E =1, χ_S =10	10	58.2	84.7

Table 5: Effect of MDE production rate (λ_M) on the time when the tumor shape parameter (S) is 1.5

Taxis Coefficients	λ_M	Low-nutrient	Nutrient-rich
χ_E =1, χ_S =0	100	33	58.5
χ_E =1, χ_S =10	10	46.5	84.8
χ_E =1, χ_S =10	100	40	58.2
χ_E =1, χ_S =10	1000	39.1	57

Table 6: Parameter values used in section 4.4

Chemotaxis coefficient, χ_S	10, 50 ,100
Surface-tension coefficient, Γ	0.01 (low surface tension) 0.05 (medium surface tension)

Table 7: Parameter values used in section 4.5

Apoptosis rate	0
Proliferation rate	0.1
Haptotaxis coefficient	0, 1, 5
Chemotaxis coefficient	0, 10, 50 ,100

[1] Macklin P, McDougall S, Anderson AR, Chaplain MA, Cristini V, Lowengrub J. Multiscale modelling and nonlinear simulation of vascular tumour growth. J Math Biol 2009;58:765-98.
[2] Cristini V, Lowengrub J, Nie Q. Nonlinear simulation of tumor growth. Journal of mathematical biology 2003;46:191-224.
[3] Zheng X, Wise S, Cristini V. Nonlinear simulation of tumor necrosis, neo-vascularization and tissue invasion via an adaptive finite-element/level-set method. Bulletin of mathematical biology 2005;67:211-59.
[4] Perumpanani AJ, Simmons DL, Gearing AJH, Miller KM, Ward G, Norbury J, et al. Extracellular matrix-mediated chemotaxis can impede cell migration. P Roy Soc B-Biol Sci 1998;265:2347-52.